

WIND TURBINE LOAD PREDICTION USING THE
BEDDOES-LEISHMAN MODEL FOR UNSTEADY
AERODYNAMICS AND DYNAMIC STALL

by

Kirk Gee Pierce

A thesis submitted to the faculty of
The University of Utah
in partial fulfillment of the requirements for the degree of

Master of Science

Department of Mechanical Engineering

The University of Utah

August 1996

Note: This Acrobat pdf file was created from the original thesis files. This copy of the thesis is complete, but some changes in pagination occurred during the conversion to a pdf file. As a result, the page numbers in the Table of Contents are not always correct.

ABSTRACT

The Beddoes-Leishman model for unsteady aerodynamics and dynamic stall has been implemented in the University of Utah's AeroDyn subroutines. These subroutines are used in determination of aerodynamic loading on wind turbine systems. At present these subroutines are used with YawDyn, a rotor analysis code developed at the University of Utah for the study of yaw loads and motions of horizontal axis wind turbines, and ADAMS[®] (Automatic Dynamic Analytic of Mechanical Systems), a commercial software package that performs multibody system analysis of mechanical systems.

This thesis presents results from validation efforts on the Beddoes model for prediction of wind turbine rotor loads. Comparisons between predicted aerodynamic force coefficients and those measured on oscillating airfoils in wind tunnels at Reynolds numbers, Mach numbers, and reduced frequencies applicable to wind turbines are presented. Comparisons are made between predicted aerodynamic force coefficients and values obtained from integration of pressure tap measurements during operation of the Combined Experiment Rotor (CER). Also, yaw motion and load predictions for the CER are compared to data.

In order to make the model applicable to the airfoils and operating environment of wind turbines some modifications to the model were necessary. The operating environment requires that the model be capable of generating aerodynamic coefficients over all angles of attack between -180° and 180° . To enable the model to generate aerodynamic

coefficients over the entire range the angle of attack was reflected about $+90^\circ$ and -90° . Also, the model must work well for general airfoil lift and drag coefficient tables. A look-up table on the separation point curve was implemented in place of a curve fit to improve the generality and increase the accuracy of the model.

Studies were performed to determine the sensitivity to changes in time constants used with the model. These studies indicate that predicted blade loads are quite insensitive to changes in the time constants associated with the model. Therefore, the constants should not need to be modified.

In general, the comparisons between measured and predicted coefficients, loads, and motions are good, indicating that the model is appropriate for the conditions encountered by wind turbines.

TABLE OF CONTENTS

ABSTRACT	iv
LIST OF FIGURES	vii
LIST OF SYMBOLS	xiv
ACKNOWLEDGMENTS	xvi
INTRODUCTION	1
METHODS	6
The Beddoes-Leishman Model	6
Model Modifications	11
RESULTS AND DISCUSSION	20
Two-Dimensional Wind Tunnel Data Simulations	20
Separation Point Shifting	21
NACA 4415 Airfoil	27
NREL S809 Airfoil	36
NASA LS(1)-0417 Airfoil	50
Comparisons to CER Data	63
Sensitivity Studies	69
CONCLUSIONS	72
APPENDICES	
A: DETERMINATION OF CONSTANTS NEEDED FOR THE MODEL	75
B: FORTRAN PROGRAM DYNSTL	79
REFERENCES	101

LIST OF FIGURES

Figure	Page
1: Dynamic stall events on a NACA 0012 airfoil, from Carr (1988).	3
2: Dynamic stall events measured at the 30% station of the CER.....	4
3: Attached flow unsteady response.	7
4: Attached flow modified by separation point.	9
5: Unsteady separation point curve.....	9
6: Attached flow, separation point, and vortex lift contribution.....	10
7: Modified angle of attack used for separation point calculation.....	11
8: Exponential curve fit to the calculated separation point data for a NACA 4415 at $Re=1.0M$	12
9: Comparison between data and reproduced curve using exponential curve fit to separation point data.	13
10: Normal and chordwise coefficient separation point curves for a NACA 4415.....	14
11: Comparison between measured and reproduced lift coefficient.....	15
12: Comparison between measured C_D , C_D reproduced using the current method, and C_D reproduced by method of Beddoes using curve fit C_N separation point.....	15
13: Dynamic normal force coefficient simulations for unusual angles of attack. $k=0.096$	16
14: Airfoils used for unsteady aerodynamic coefficient comparisons.....	21
15: NACA 4415 lift coefficient versus angle of attack. High amplitude oscilla- tion. $\alpha=19.7+9.8\sin(\omega t)$, $k=0.096$, $M=0.1$	22

16: NACA 4415 drag coefficient versus angle of attack. Conditions as given in Figure 15.	22
17: NACA 4415 lift coefficient versus angle of attack. Low amplitude oscillation. $\alpha=20.2+3.2\sin(\omega t)$, $k=0.087$, $M=0.1$	23
18: NACA 4415 drag coefficient versus angle of attack. Conditions as given in Figure 17.	23
19: NACA 4415 lift coefficient versus angle of attack. High amplitude oscillation. $\alpha=19.7+9.8\sin(\omega t)$, $k=0.096$, $M=0.1$ Shown are the effects of separation point time constant increase for decreasing angle of attack.	25
20: NACA 4415 drag coefficient versus angle of attack. Conditions as given in Figure 19.	25
21: NACA 4415 lift coefficient versus angle of attack. Low amplitude oscillation. $\alpha=20.2+3.2\sin(\omega t)$, $k=0.087$, $M=0.1$ Shown are the effects of separation point time constant increase for decreasing angle of attack.	26
22: NACA 4415 drag coefficient versus angle of attack. Conditions as given in Figure 21.	26
23: NACA 4415 lift coefficient versus angle of attack. $\alpha=14+10\sin(\omega t)$, $k=0.029$, $M=0.09$	28
24: NACA 4415 drag coefficient versus angle of attack. Conditions as given in Figure 23.	28
25: NACA 4415 lift coefficient versus angle of attack. $\alpha=14+10\sin(\omega t)$, $k=0.055$, $M=0.09$	29
26: NACA 4415 drag coefficient versus angle of attack. Conditions as given in Figure 25.	29
27: NACA 4415 lift coefficient versus angle of attack. $\alpha=14+10\sin(\omega t)$, $k=0.086$, $M=0.09$	30
28: NACA 4415 drag coefficient versus angle of attack. Conditions as given in Figure 27.	30
29: NACA 4415 lift coefficient versus angle of attack. $\alpha=20+10\sin(\omega t)$, $k=0.031$, $M=0.08$	31
30: NACA 4415 drag coefficient versus angle of attack. Conditions as given in Figure 29.	31

31: NACA 4415 lift coefficient versus angle of attack. $\alpha=20+10\sin(\omega t)$, k=0.064, M=0.08	32
32: NACA 4415 drag coefficient versus angle of attack. Conditions as given in Figure 31.	32
33: NACA 4415 lift coefficient versus angle of attack. $\alpha=20+10\sin(\omega t)$, k=0.096, M=0.08	33
34: NACA 4415 drag coefficient versus angle of attack. Conditions as given in Figure 33.	33
35: Chordwise force coefficient versus angle of attack. Conditions as given in Figure 33. Simulated hysteresis does not stall as rapid as measured val- ues.	35
36: Chronology of measured aerodynamic coefficients. Conditions as given in Figure 33.	35
37: NACA 4415 lift coefficient versus angle of attack. $\alpha=8+3.5\sin(\omega t)$, k=0.059, M=0.09	37
38: NACA 4415 drag coefficient versus angle of attack. Conditions as given in Figure 37.	37
39: NACA 4415 lift coefficient versus angle of attack. $\alpha=8+3.5\sin(\omega t)$, k=0.089, M=0.09	38
40: NACA 4415 drag coefficient versus angle of attack. Conditions as given in Figure 39.	38
41: NACA 4415 lift coefficient versus angle of attack. $\alpha=20+3.5\sin(\omega t)$, k=0.087, M=0.09	39
42: NACA 4415 drag coefficient versus angle of attack. Conditions as given in Figure 41.	39
43: NREL S809 lift coefficient versus angle of attack. $\alpha=20+10\sin(\omega t)$, k=0.025, M=0.1	40
44: NREL S809 drag coefficient versus angle of attack. Conditions as given in Figure 43.	40
45: NREL S809 lift coefficient versus angle of attack. $\alpha=20+10\sin(\omega t)$, k=0.051, M=0.1	41

46: NREL S809 drag coefficient versus angle of attack. Conditions as given in Figure 45.	41
47: NREL S809 lift coefficient versus angle of attack. $\alpha=20+10\sin(\omega t)$, $k=0.078$, $M=0.1$	42
48: NREL S809 drag coefficient versus angle of attack. Conditions as given in Figure 47.	42
49: NREL S809 lift coefficient versus angle of attack. $\alpha=14+10\sin(\omega t)$, $k=0.026$, $M=0.1$	43
50: NREL S809 drag coefficient versus angle of attack. Conditions as given in Figure 49.	43
51: NREL S809 lift coefficient versus angle of attack. $\alpha=20+10\sin(\omega t)$, $k=0.053$, $M=0.1$	44
52: NREL S809 drag coefficient versus angle of attack. Conditions as given in Figure 51.	44
53: NREL S809 lift coefficient versus angle of attack. $\alpha=14+10\sin(\omega t)$, $k=0.080$, $M=0.1$	45
54: NREL S809 drag coefficient versus angle of attack. Conditions as given in Figure 53.	45
55: NREL S809 lift coefficient versus angle of attack. $\alpha=8+10\sin(\omega t)$, $k=0.026$, $M=0.1$	46
56: NREL S809 drag coefficient versus angle of attack. Conditions as given in Figure 55.	46
57: NREL S809 lift coefficient versus angle of attack. $\alpha=8+10\sin(\omega t)$, $k=0.053$, $M=0.1$	47
58: NREL S809 drag coefficient versus angle of attack. Conditions as given in Figure 57.	47
59: NREL S809 lift coefficient versus angle of attack. $\alpha=8+10\sin(\omega t)$, $k=0.077$, $M=0.1$	48
60: NREL S809 drag coefficient versus angle of attack. Conditions as given in Figure 59.	48
61: NREL S809 chordwise force coefficient versus angle of attack. Conditions as given in Figure 59.	50

62: NASA LS(1)-0417 lift coefficient versus angle of attack. $\alpha=20+10\sin(\omega t)$, k=0.027, M=0.1	51
63: NASA LS(1)-0417 drag coefficient versus angle of attack. Conditions as given in Figure 62.	51
64: NASA LS(1)-0417 lift coefficient versus angle of attack. $\alpha=20+10\sin(\omega t)$, k=0.055, M=0.1	52
65: NASA LS(1)-0417 drag coefficient versus angle of attack. Conditions as given in Figure 64.	52
66: NASA LS(1)-0417 lift coefficient versus angle of attack. $\alpha=20+10\sin(\omega t)$, k=0.081, M=0.1	53
67: NASA LS(1)-0417 drag coefficient versus angle of attack. Conditions as given in Figure 66.	53
68: Chordwise force coefficient versus angle of attack. Conditions given in Figure 66. Predicted C_C does not stall as rapidly as the data.....	54
69: NASA LS(1)-0417 lift coefficient versus angle of attack. $\alpha=14+10\sin(\omega t)$, k=0.026, M=0.1	55
70: NASA LS(1)-0417 drag coefficient versus angle of attack. Conditions as given in Figure 69.	55
71: NASA LS(1)-0417 lift coefficient versus angle of attack. $\alpha=14+10\sin(\omega t)$, k=0.052, M=0.1	56
72: NASA LS(1)-0417 drag coefficient versus angle of attack. Conditions as given in Figure 71.	56
73: NASA LS(1)-0417 lift coefficient versus angle of attack. $\alpha=14+10\sin(\omega t)$, k=0.079, M=0.1	57
74: NASA LS(1)-0417 drag coefficient versus angle of attack. Conditions as given in Figure 73.	57
75: NASA LS(1)-0417 lift coefficient versus angle of attack. $\alpha=8+10\sin(\omega t)$, k=0.026, M=0.1	58
76: NASA LS(1)-0417 drag coefficient versus angle of attack. Conditions as given in Figure 75.	58
77: NASA LS(1)-0417 lift coefficient versus angle of attack. $\alpha=8+10\sin(\omega t)$, k=0.052, M=0.1	59

78: NASA LS(1)-0417 drag coefficient versus angle of attack. Conditions as given in Figure 77.	59
79: NASA LS(1)-0417 lift coefficient versus angle of attack. $\alpha=8+10\sin(\omega t)$, $k=0.082$, $M=0.1$	60
80: NASA LS(1)-0417 drag coefficient versus angle of attack. Conditions as given in Figure 79.	60
81: Chordwise force coefficient versus angle of attack. Conditions as given in Figure 79.	61
82: Four minute YawDyn prediction of yaw angle for the CER with a mean wind velocity of 12 m/s, 72 rpm.	63
83: 80% radius normal force coefficient comparison. Conditions as given in Figure 82.	64
84: 80% radius root mean square (RMS) angle of attack versus reduced frequency for the four minutes of data used in Figure 82.	65
85: 80% radius normal force coefficient comparison. Conditions as given in Figure 82.	65
86: Initial prediction of normal force coefficient at the 30% station. Conditions as given in Figure 82.	66
87: Due to delayed static stall measured operating data remain well above static data.	67
88: Angle of attack indicator is seen to “ring” after passing through tower shadow.	68
89: Comparison between predicted and measured normal force coefficients using the modified static curve. Conditions as given in Figure 82.	69
90: Root flap bending moment rainflow counts for 30% increase in time constants.	71
91: Root flap bending moment rainflow counts for 30% decrease in time constants.	72
92: Determination of parameters for the NASA LS(1)-0417 airfoil.	77
93: Determination of parameters for the NREL S809 airfoil.	77
94: Determination of parameters for the NACA 4415 airfoil.	78

LIST OF SYMBOLS

c	Chord length
C_C	Chordwise force coefficient
C_D	Drag force coefficient
C_{D0}	Minimum drag force coefficient
C_L	Lift force coefficient
C_M	Moment force coefficient
C_N	Normal force coefficient
C'_N	First order lagged normal force coefficient
C_{N1}	Normal force coefficient value at stall
C_{N1L}	Normal force coefficient value at negative stall
$C_{N\alpha}$	Normal force coefficient slope near 0° angle of attack
C_N^C	Circulatory component of normal force coefficient
C_N^I	Noncirculatory component of normal force coefficient
f	Nondimensional separation point, Nondimensional effective separation point
k	Reduced frequency = $\omega c/(2V)$
M	Mach number
T_p	Time constant for first order lag in pressure due to unsteady flow
T_f	Time constant of first order lag applied to motion of the separation point

T_v	Time constant governing strength of dynamic stall vortex
T_{vl}	Nondimensional time of transit for the vortex moving across the airfoil surface
V	Local flow velocity
x	Point of flow separation on airfoil
α	Angle of attack
α_0	Zero lift angle of attack
α_m	Modified angle of attack
ϕ_α^C	Circulatory indicial function
ϕ_α^I	Noncirculatory indicial function
Φ	Chordwise force coefficient correction parameter for large angles of attack
τ_v	Nondimensional position of dynamic stall vortex
ω	Circular frequency

ACKNOWLEDGMENTS

I would like to thank Dr. Craig Hansen for his patience, guidance and support during the research and writing of this thesis. I would also like to thank friends and family who have given support and inspiration during this work. Finally, I would like to thank the National Renewable Energy Laboratory (NREL) which made this research possible.

INTRODUCTION

The accurate prediction of wind turbine loading is necessary to reduce the risks involved in producing a new machine, and to reduce the cost of manufacturing and maintaining the turbine. This, in turn, reduces the cost of energy generated by the wind turbine making it more competitive with nonrenewable energy sources. According to the American Wind Energy Association, turbines are producing energy for 5 cents per kWh in 1995, and costs may drop to 3 cents per kWh by the year 2000. Improvement in the understanding of wind turbine loading and systems is necessary if the wind industry is to reach this goal.

Inaccurate predictions of wind turbine power and structural loads have led to insufficient design of wind turbine components, and premature failures. A 20- to 30- year turbine life is necessary to enable wind power to compete with nonrenewable energy sources. Significant improvements in load prediction have been made in the last 15 years, however there is still much research needed before many of the physical mechanisms affecting the aerodynamics of wind turbines are understood. Present design codes underpredict the amount of power generated during high wind speeds on stall controlled machines. Also structural loads have been underpredicted, leading to failures of yaw drive components, low speed shafts, and blades. Some of the underpredictions have been attributed to three-dimensional aerodynamic effects and dynamic stall. The flow field of a wind turbine is very three-dimensional. Centrifugal pumping and Coriolis accelerations

lead to a delay of stall at the inboard blade sections (Hansen and Butterfield, 1993). This delayed static stall produces much higher lift than predicted, resulting in an increase of turbine power and loading.

Load underprediction has also been attributed to dynamic stall. Dynamic stall is the term used to describe the complex events that result in the delay of stall on airfoils undergoing periodic or general unsteady motion. For an airfoil oscillating or pitching through the static stall angle of attack, the onset of stall can be delayed to angles of attack considerably in excess of the static stall angle. However, when the airfoil does stall, the stall is more severe, and for oscillating airfoils, persists to lower angles of attack than the static stall. After stall, the flow begins to reattach to the airfoil from front to rear. This delay of stall during increasing pitch, followed by strong stall, produces large hysteresis in the aerodynamic forces on the airfoil. Thus, in contrast to steady aerodynamics, the coefficients of lift, drag, and moment, are not unique functions of angle of attack, but depend on a number of other parameters such as reduced frequency, mean angle of attack, and amplitude of oscillation.

One cycle of an airfoil undergoing dynamic stall is illustrated in Figure 1. The chronology of events for an airfoil that stalls from the trailing edge, pitching through the static stall angle, is as follows. As the pitching airfoil passes through the static stall angle there is no discernible change in the viscous or inviscid flow about the airfoil. This is due to the finite time required for the stall events to occur. The first noticeable disturbance to occur is flow reversal in the boundary layer near the trailing edge. This flow reversal then proceeds toward the leading edge of the airfoil until flow reversal occurs over most of the chord. Large eddies appear in the boundary layer and a vortex forms

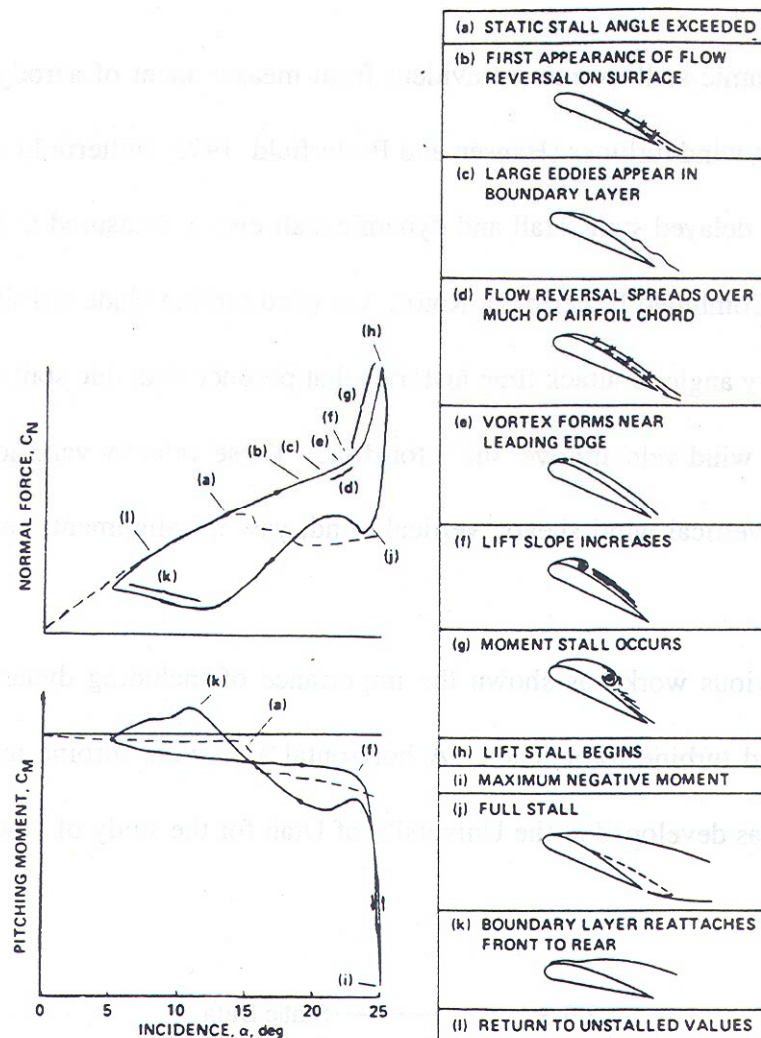


Figure 1: Dynamic stall events on a NACA 0012 airfoil, from Carr (1988).

near the leading edge. This vortex gains in strength, then convects over the airfoil at a speed of approximately 0.3 times the free-stream velocity (Chandrasekhara and Carr, 1990).

As the vortex moves across the airfoil the center of pressure moves with it causing a large nose-down pitching moment. After the vortex has passed the trailing edge, the airfoil experiences severe stall, with lift coefficient values often falling well below the static stall values. After full stall, as the angle of attack falls below the static stall value,

the flow begins to reattach from front to rear, until unstalled values of aerodynamic force coefficients are again obtained.

Dynamic stall events are evident from measurement of aerodynamic coefficients on operating wind turbines (Hansen and Butterfield, 1993, Butterfield et al, 1991). Figure 2 illustrates delayed static stall and dynamic stall events measured at the 30% span location of the Combined Experiment Rotor. On wind turbine blade airfoil sections, unsteady or oscillatory angle of attack time histories that produce dynamic stall events occur due to variation in wind velocity over the rotor disk. These velocity variations are due to horizontal and vertical wind shears, vertical wind, yaw misalignment, and turbulence in the wind.

Previous work has shown the importance of including dynamic stall when predicting wind turbine rotor loads. A horizontal axis wind turbine analysis code named

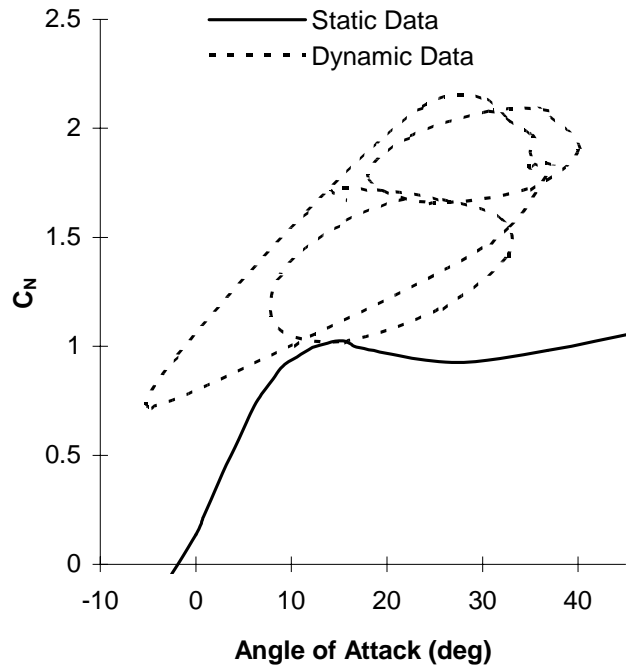


Figure 2: Dynamic stall events measured at the 30% station of the CER.

YawDyn was developed at the University of Utah for the study of yaw loads and motions of wind turbines. The YawDyn code is described in detail in other references (Hansen, 1992, Hansen et al., 1990). YawDyn predictions of Combined Experiment Rotor (CER) loads were improved by the addition of the Gormont dynamic stall model (Hansen, 1992, Hansen et al., 1990).

In the present work the Beddoes dynamic stall model was added to the AeroDyn subroutines due to short-comings that were observed with the Gormont model. Hansen found that key coefficients in the Gormont model needed to be changed in order to reproduce the measured CER lift coefficient hysteresis and the measured yaw moment. The Gormont model also required a filter on the angle of attack to stabilize lift coefficient predictions due to noise in the time rate of change of the angle of attack. The Beddoes model is semiempirical, being based on airfoil indicial response. Indicial response produces the lift and pitching moment on an airfoil due to a step change in angle of attack and is derived from the linearized differential equations for an unsteady, compressible, inviscid fluid. Therefore, it is based on the physics of the flow, rather than on purely empirical relations. In contrast, the Gormont model is purely empirical. It was hoped that the Beddoes model would be more applicable to the environment encountered by, and the airfoils used for, wind turbines without the need to modify constants or filter the angle of attack.

Recently, computational fluid dynamics has been able to determine the aerodynamic response of an airfoil for a given motion (Tuncer et al., 1990). However, the solutions are complex and require considerable computation time. For these reasons present

design codes use empirical or semiempirical models for representation of the unsteady airloads, and will continue to do so in the near future.

METHODS

The Beddoes-Leishman Model

For a detailed description of the Beddoes-Leishman model for unsteady aerodynamics and dynamic stall see Beddoes (1983, 1984), Leishman and Beddoes (1986, 1989), and Leishman (1988, 1989, 1990). A brief description will be given here.

The Beddoes-Leishman model is a semiempirical model that is based on airfoil indicial response. Indicial response produces the normal force coefficient (C_N), and the moment force coefficient (C_M) as a function of time for a step change in angle of attack. The indicial response is derived from solution of the linearized differential equations for an unsteady, compressible, inviscid fluid (Bisplinghoff et al., 1955). The increment in C_N due to a step change in angle of attack ($\Delta\alpha$) is broken into two components, a non-circulatory component (C_N^I), and a circulatory component (C_N^C), given as:

$$\begin{aligned}\Delta C_N^C &= C_{N\alpha} \phi_\alpha^C \Delta\alpha \\ \Delta C_N^I &= \frac{4}{M} \phi_\alpha^I \Delta\alpha\end{aligned}\tag{1}$$

where $C_{N\alpha}$ is the normal force coefficient curve slope, M is the Mach number, ϕ_α^C is the circulatory indicial function, and ϕ_α^I is the noncirculatory indicial function. These indicial functions are nearly pure exponential functions, and are represented by exponential functions in the model. In the Beddoes-Leishman model the chordwise force coefficient (C_C) response is based on the circulatory component of C_N . The airfoil attached flow

response due to a general angle of attack history is calculated from the superposition of individual indicial responses for each step. The attached flow C_N hysteresis is shown in Figure 3.

The calculated attached flow response is then modified based on the position of the effective flow separation point on the low pressure side of the airfoil. Flow separation from the airfoil results in a loss of circulation about the airfoil, reducing aerodynamic coefficients from the attached flow values. The separation point is given by $f = x / c$, where x is the point of flow separation measured from the leading edge, and c is the airfoil chord length. An approximation to Kirchhoff theory (Thwaites, 1960) used by Beddoes relates C_N and C_C to the separation point given as:

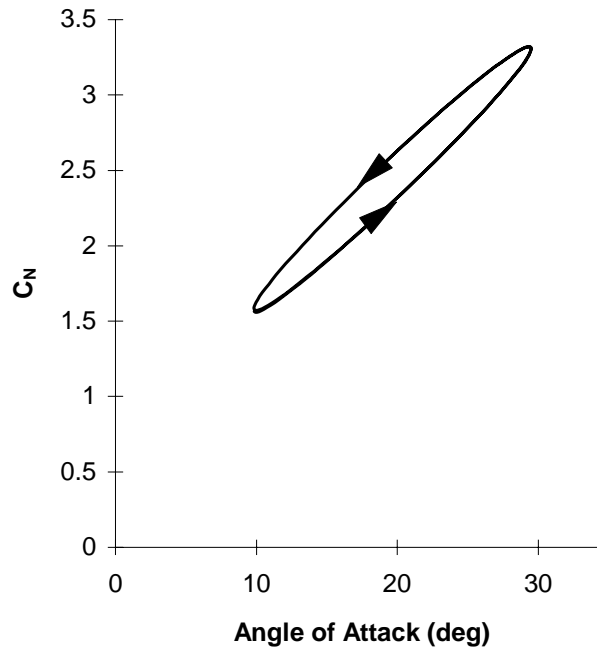


Figure 3: Attached flow unsteady response.

$$\begin{aligned}
C_N &= C_{N\alpha} (\alpha - \alpha_0) \left(\frac{1 + \sqrt{f}}{2} \right)^2 \\
C_C &= C_{N\alpha} (\alpha - \alpha_0) \tan(\alpha) \sqrt{f}
\end{aligned} \tag{2}$$

where α is the angle of attack, and α_0 is the zero-lift angle of attack.

The static effective separation point is calculated from static C_N data by solving equation 2. The effective separation point versus angle of attack is then curve fit using an exponential function. f calculated from equation 2 using static data is referred to as the effective separation point since it represents the amount of separation according to Kirchoff theory, which is a inviscid solution, but may not necessarily represent the actual point of flow reversal on the airfoil. It does however provide a method of representing the effect and dynamics of separation. In the Beddoes model an empirically derived first order lag is applied to the movement of the effective separation point to account for the time lag in movement of the separation point during unsteady conditions. Figure 4 shows the calculated C_N including the effects of unsteady separation. The unsteady effective separation point curve is shown in Figure 5.

The final main component of the model represents the vortex buildup and shedding that occurs during dynamic stall. The vortex lift contribution is empirically modeled as an excess circulation in the vicinity of the airfoil. The magnitude of the increase in lift is based on the difference between the attached flow C_N , and the C_N value obtained from the Kirchoff equation. Empirically derived time constants are used to govern the growth, decay, and motion of the vortex. As the airfoil pitches upward the vortex strength is allowed to build. When the first order lagged attached flow C_N (C_N') exceeds the C_N

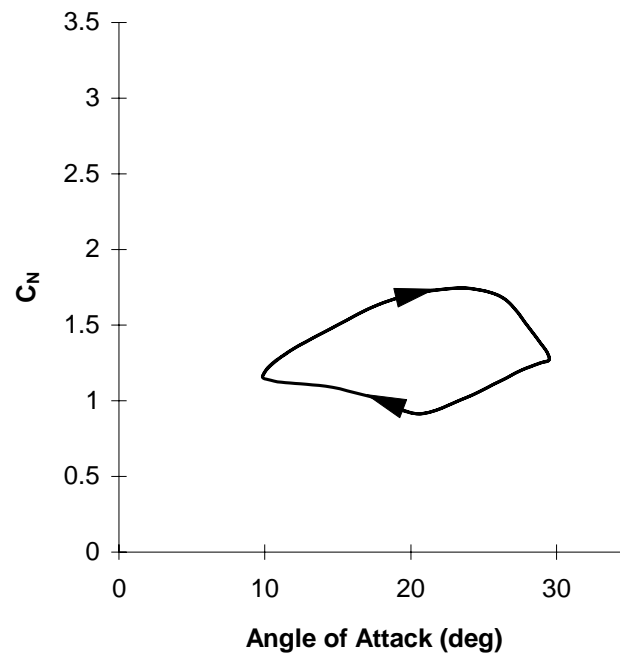


Figure 4: Attached flow modified by separation point.

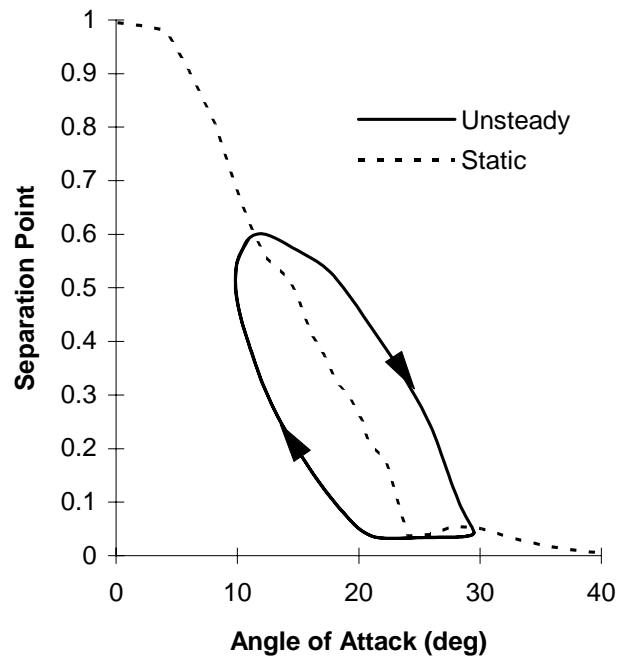


Figure 5: Unsteady separation point curve.

value at stall (C_{N_i}) the vortex is allowed to begin convecting across the airfoil. A nondimensional time constant (τ_v) tracks the position of the vortex across the airfoil. As the vortex reaches the trailing edge the strength is allowed to decay exponentially. The calculated C_N including all model components is shown in Figure 6.

The lift coefficient (C_L) and drag coefficient (C_D) are then calculated from resolving C_N and C_C into components normal and parallel to the velocity direction, and adding the minimum drag (C_{D0}).

$$\begin{aligned} C_L &= C_N \cos(\alpha) + C_C \sin(\alpha) \\ C_D &= C_N \sin(\alpha) - C_C \cos(\alpha) + C_{D0} \end{aligned} \quad (3)$$

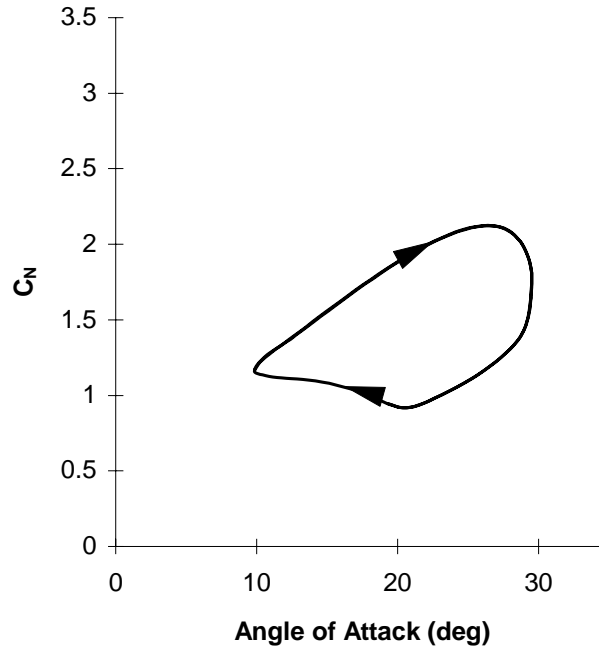


Figure 6: Attached flow, separation point, and vortex lift contribution.

Model Modifications

Some modifications to the model were necessary to make it applicable to the environment and airfoils of wind turbines. Beddoes considers angles of attack from approximately -10° to 30° ; however wind turbine airfoils often operate outside of this range. The operating environment of wind turbines requires that the model be capable of producing aerodynamic force coefficients over the entire range of possible angles of attack. To accomplish this several modifications to the model were necessary.

To allow the model to reproduce aerodynamic coefficients at high angles of attack, the angle of attack was modified as follows:

$$\begin{aligned} \text{for } |\alpha| \leq 90^\circ \quad \alpha_m &= \alpha \\ \alpha > 90^\circ \quad \alpha_m &= 180^\circ - \alpha \\ \alpha < -90^\circ \quad \alpha_m &= -180^\circ - \alpha \end{aligned} \tag{4}$$

where α is the current angle of attack and α_m is the modified angle of attack. The modified angle of attack is shown in Figure 7. The modified angle of attack represents the fact

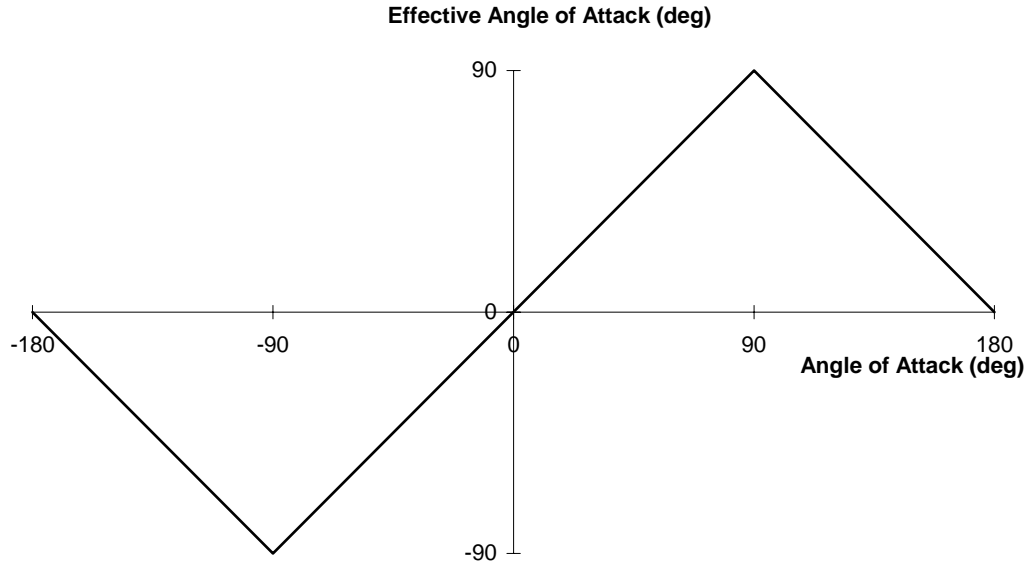


Figure 7: Modified angle of attack used for separation point calculation.

that the normal force coefficient is somewhat symmetric about $+90^\circ$ and -90° . The modified angle of attack is used to calculate the effective separation point from the Kirchhoff equation, and is also used for runtime calculation of the attached flow response.

As mentioned previously Beddoes uses an exponential curve fit to the effective airfoil separation point calculated from the static data using equation 2, and shown in Figure 8. However this did not work well with some of the airfoils tested. As can be seen in Figure 9, some important features are lost when regenerating the C_N versus angle of attack curve using the exponential curve fit representation of the effective separation point. For this reason a lookup table was used, in which the calculated effective separation point values are stored with angle of attack values. Linear interpolation is used between points. This method is more applicable to any airfoil and accurately reproduces

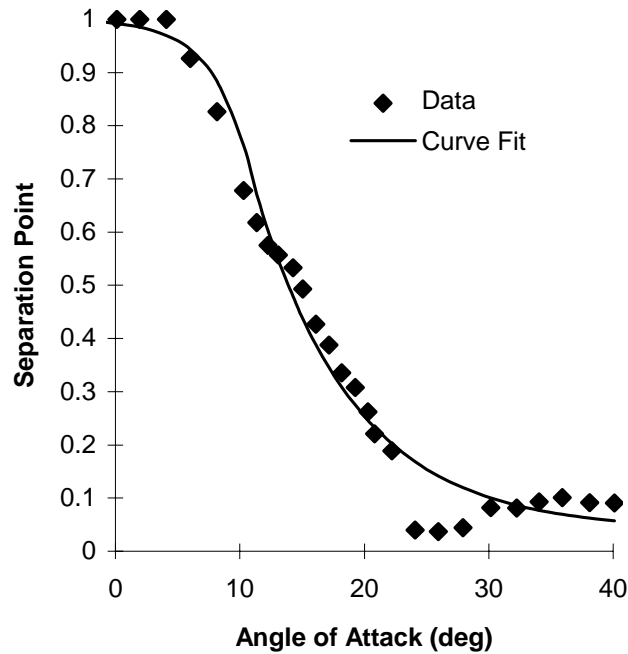


Figure 8: Exponential curve fit to the calculated separation point data for a NACA 4415 at $Re=1.0M$.

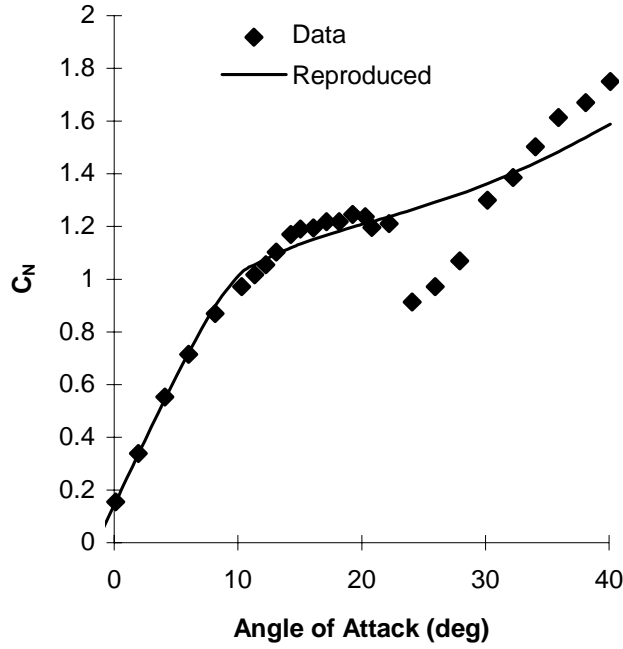


Figure 9: Comparison between data and reproduced curve using exponential curve fit to separation point data.

the normal force curve.

Also upon further investigation into the model it was determined that the calculated C_c value, which was based upon the circulatory component of C_N and the effective separation point calculated using C_N , at times did not reproduce static values. In some angle of attack ranges higher or lower drag was predicted by the model due to an error in prediction of C_c . This resulted in erroneous power output predictions for the rotor. To alleviate this problem two effective separation point tables are calculated, one for C_N and one for C_c . Equation 2 for C_c is used for calculation of the C_c effective separation point table representing the separation affecting C_c according to Kirchhoff theory. It is also used for runtime calculation of C_c using the dynamic effective C_c separation point. During unsteady conditions the same dynamics are applied to each effective separation

point. This method allows the model to accurately reproduce static values for very general input values of C_L and C_D .

For most airfoils the two tables are similar, however at times there are differences between the two, and even small differences can lead to a significant error in the drag prediction. Figure 10 shows the two effective separation point curves. The model using two effective separation point tables accurately reproduces the static aerodynamic coefficients, as shown in Figures 11 and 12. Also the dynamic values compare well to those measured in wind tunnel tests, as will be shown in the results section.

In Figure 13 dynamic stall hysteresis loops are shown for unusual angle of attack ranges as calculated by the modified method. Although the accuracy of the model for high angles of attack is not known, because of the lack of test data, the results obtained are at least reasonable.

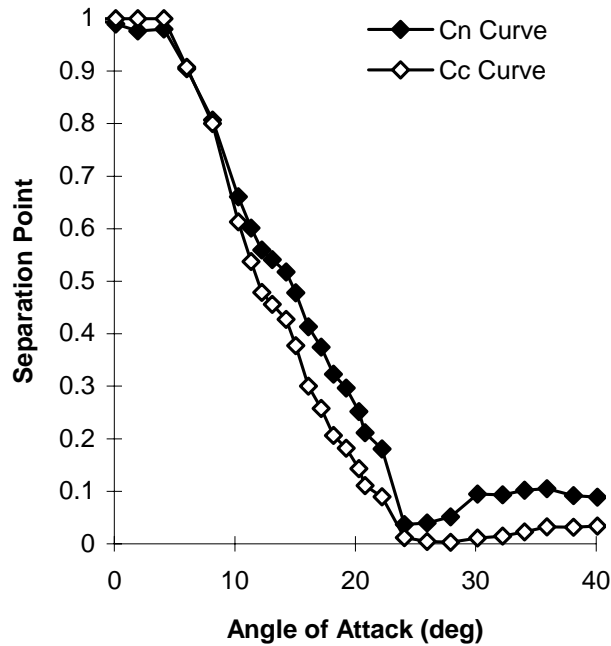


Figure 10: Normal and chordwise coefficient separation point curves for a NACA 4415.

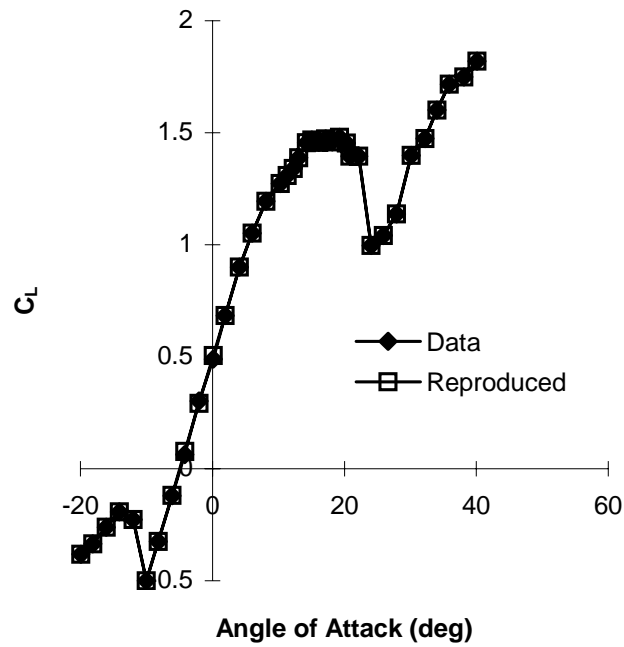


Figure 11: Comparison between measured and reproduced lift coefficient.

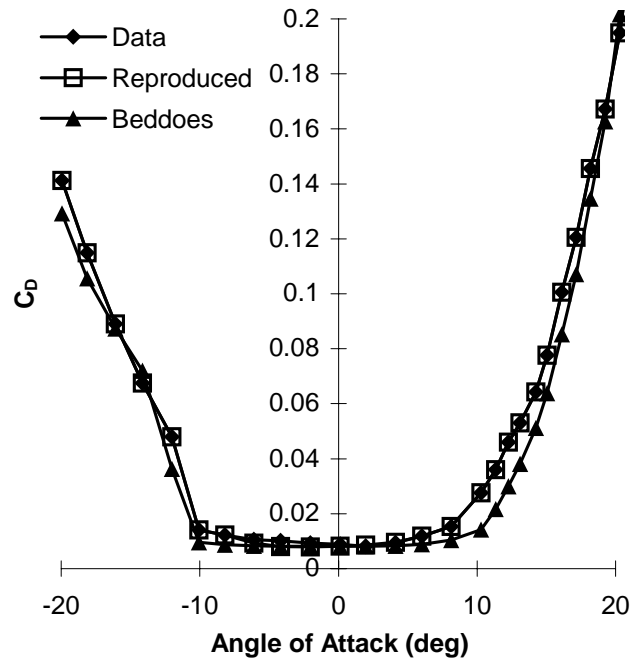


Figure 12: Comparison between measured C_D , C_D reproduced using the current method, and C_D reproduced by method of Beddoes using curve fit C_N separation point.

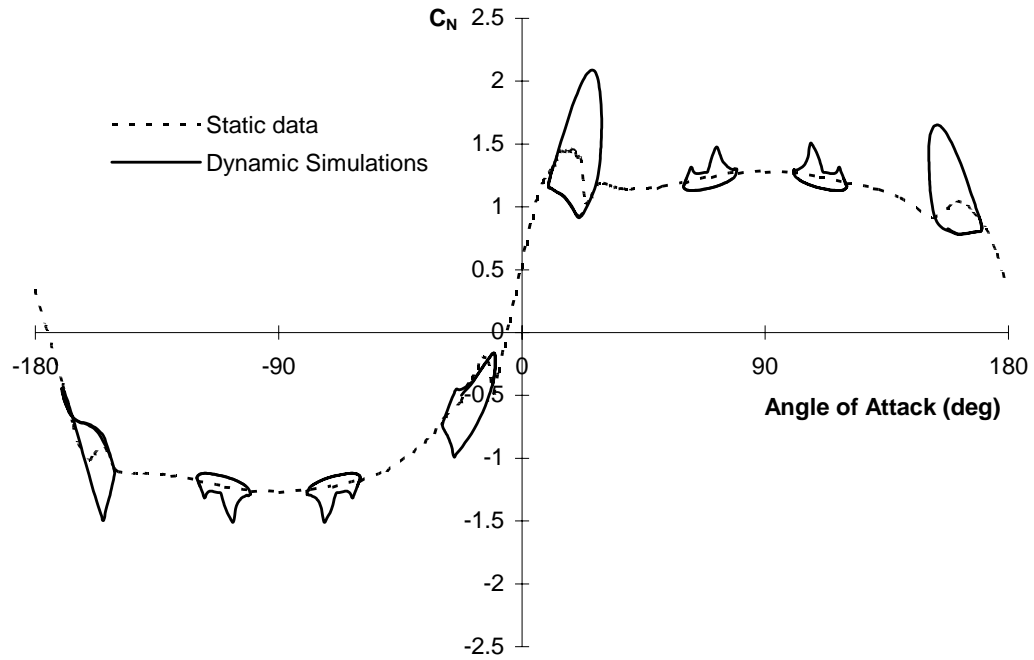


Figure 13: Dynamic normal force coefficient simulations for unusual angles of attack.
 $k=0.096$

At angles of attack near $+90^\circ$ and -90° , and occasionally at other locations, the square root of the effective separation point in equation 2 should be negative to reproduce static aerodynamic coefficient values. This created problems in regenerating the aerodynamic force coefficients since the negative sign is lost when squaring the value to determine the effective separation point. To eliminate this problem, and to ensure proper regeneration of coefficients, the sign of the effective separation point is saved with the value of the parameter. The sign is then used when regenerating aerodynamic coefficients to ensure accurate regeneration. The process of decomposition of the C_N is shown below in equation 5, with the regeneration given by equation 6.

$$t = 4 \sqrt{\frac{C_N}{C_{N\alpha}(\alpha - \alpha_0)}} - 1$$

$$f = t^2 \text{sign}(t)$$
(5)

$$C_N = C_{N\alpha}(\alpha - \alpha_0) \left(\frac{1 + \sqrt{\text{abs}(f) \text{sign}(f)}}{2} \right)^2$$
(6)

Similarly for the C_c the process of decomposition is shown below in equation 7, with the regeneration given by equation 8.

$$t = \frac{C_c}{C_{N\alpha}(\alpha - \alpha_0)\alpha}$$

$$f_c = t^2 \text{sign}(t)$$
(7)

$$C_c = C_{N\alpha}(\alpha - \alpha_0)\alpha \sqrt{\text{abs}(f_c) \text{sign}(f_c)}$$
(8)

Beddoes also includes an empirical separation point shift for the "deep stall regime." However, whether or not this shifting increases or decreases accuracy depends on the amplitude of oscillation of the airfoil. For high amplitude oscillations increased accuracy was obtained by including the shift. However, for low amplitude oscillations better accuracy was obtained without the shift. Also, the shifting was found to cause discontinuities and hence numerical instabilities in YawDyn and ADAMS force calculations for very small angle of attack oscillation amplitudes. For these reasons the shifting has been removed from the model used in AeroDyn. This shifting will be discussed further in the results section.

For extension to deep stall Beddoes and Leishman include an additional parameter, Φ , for correction of the chordwise force during large separations. However, with the current formulation of two effective separation point tables the use of this additional modification seems unnecessary.

Another modification needed is due to parameters that must be triggered and re-initialized at certain locations in the hysteresis. The parameters determine if the vortex strength is building, the time at which the dynamic stall vortex begins to convect over the airfoil, and the position of the vortex. The difficulty arises during general unsteady motion, and at unusual angles of attack when it is unclear whether vortex lift should be added, and when parameters should be reinitialized. As mentioned previously the vortex is allowed to build in strength as the airfoil pitches toward stall ($+90^\circ$ or -90°). The change in C'_N from one step to the next is used to determine if the airfoil is pitching toward stall. If C'_N is increasing toward stall a parameter is set to allow the vortex strength to build. C'_N is used since it is less subject to noise than the angle of attack.

The vortex begins to convect across the airfoil when C'_N exceeds C_{N_1} . At this time a flag is triggered and the nondimensional parameter τ_v tracks the position of the vortex across the airfoil. τ_v starts at 0 when C'_N exceeds C_{N_1} , and increases to 1 when the vortex reaches the trailing edge. After the vortex has passed the trailing edge ($\tau_v > 1$) the vortex strength decays with a time constant equal to half of the value used during accumulation with no further additions to the vortex strength. τ_v is reset to 0 if the airfoil begins pitching toward stall after completing a cycle, the angle of attack changes sign, or after a suitable time delay if the airfoil continues pitching toward stall to allow a secondary vortex to develop and shed using the same dynamics. The frequency of shedding corresponds closely to a Strouhal number of 0.2 (Leishman and Beddoes, 1986). If C'_N does not exceed C_{N_1} the vortex strength decays as the airfoil pitches away from stall using a time constant equal to half of the value used during accumulation.

The final modification is due to the effect of the vortex component on C_C . As mentioned previously C_C is based on the circulatory component of C_N . However Beddoes and Leishman do not state whether the vortex component, which is circulatory, should be included in the calculation of C_C . From study of unsteady data it was apparent that the vortex component contributed to C_C . To model this contribution the vortex component of C_N was added to C_C in the same manner as the circulatory component of C_N , but also multiplied by $(1 - \tau_v)$. The vortex component was multiplied by $(1 - \tau_v)$ since the effect of the vortex on C_C should depend on the location of the vortex along the chord. Thus the vortex contributes to C_C in the same manner as the circulatory component of C_N when near the leading edge of the airfoil, but goes to zero as the vortex reaches the trailing edge. This method produced good agreement with the test data.

RESULTS AND DISCUSSION

Two-Dimensional Wind Tunnel Data Simulations

Although the flow field encountered by wind turbines is far from two-dimensional, it is necessary for the model to accurately reproduce two-dimensional wind tunnel data if there is any hope of representing the complex flow encountered by wind turbines. Simulations of lift and drag coefficients were performed using data obtained from Ohio State University (Gregorek and Reuss, 1992, 1994), which was taken using airfoils, Reynolds numbers, and reduced frequencies applicable to wind turbine rotors. Simulations showing the effect of the aforementioned shift are also presented.

The airfoils used for the comparisons are the NACA 4415, the NASA LS(1)-0417 MOD, and the NREL S809. The airfoil shapes are shown in Figure 14. The NACA 4415 is a standard section, the LS(1)-0417 is a low Reynolds number airfoil, and the S809 is an airfoil designed specifically for wind turbine use by the National Renewable Energy Laboratory (NREL). The data used in the comparisons were for a smooth airfoil at a Reynolds number of about 1 million, with reduced frequencies between approximately 0.02 and 0.1.

There are several time constants associated with the Beddoes model, as mentioned previously. In general the user of the code may not have access to unsteady data, or if they do, may not have the knowledge of how to modify the constants. Therefore, it is hoped that these constants are somewhat universal, capable of producing quite accurate

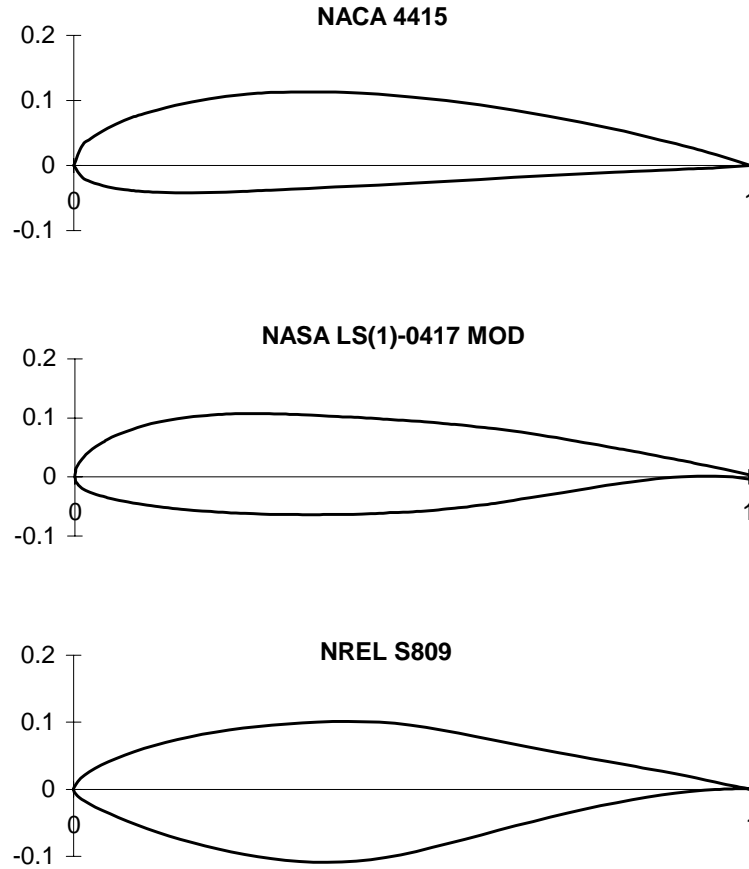


Figure 14: Airfoils used for unsteady aerodynamic coefficient comparisons.

aerodynamic force coefficients for general airfoil shapes and operating environments. From the studies performed on these three airfoil sections it appears that this is the case. The same time constants were used for each of the airfoil sections studied, and generally produced quite accurate predictions of C_L and C_D for each.

Separation Point Shifting

Figures 15 through 18 are comparisons between predicted and measured lift and drag curves for a NACA 4415. The conditions for the comparisons are given in the figures. α is the angle of attack in degrees, ω is the circular frequency, M is the Mach num-

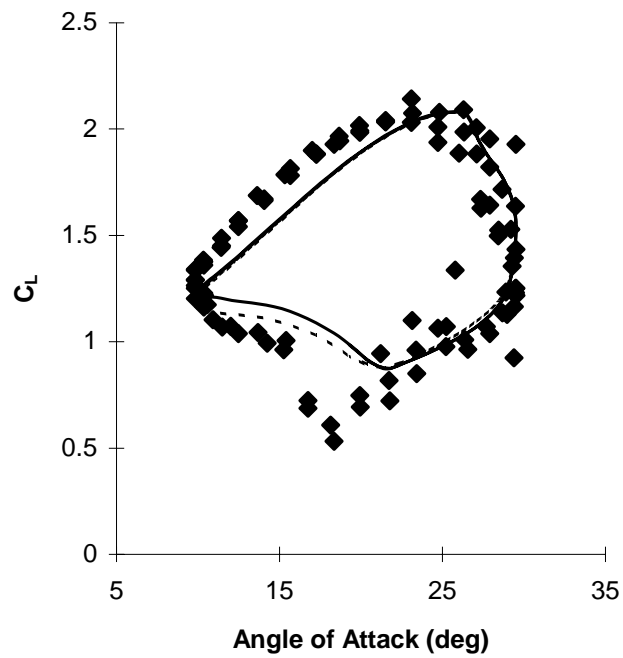


Figure 15: NACA 4415 lift coefficient versus angle of attack. High amplitude oscillation.
 $\alpha=19.7+9.8\sin(\omega t)$, $k=0.096$, $M=0.1$

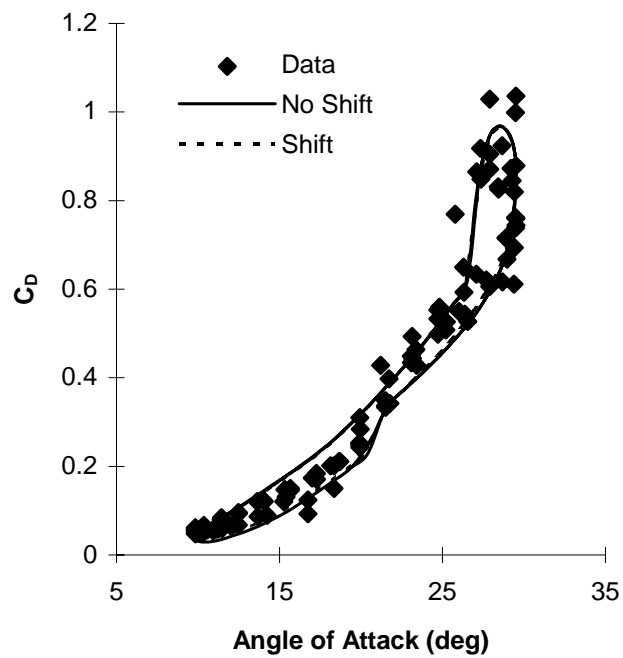


Figure 16: NACA 4415 drag coefficient versus angle of attack. Conditions as given in Figure 15.

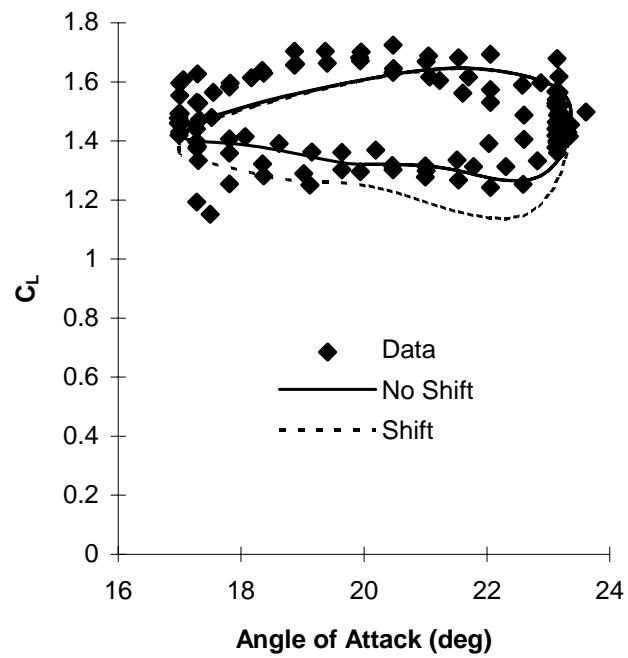


Figure 17: NACA 4415 lift coefficient versus angle of attack. Low amplitude oscillation.
 $\alpha=20.2+3.2\sin(\omega t)$, $k=0.087$, $M=0.1$

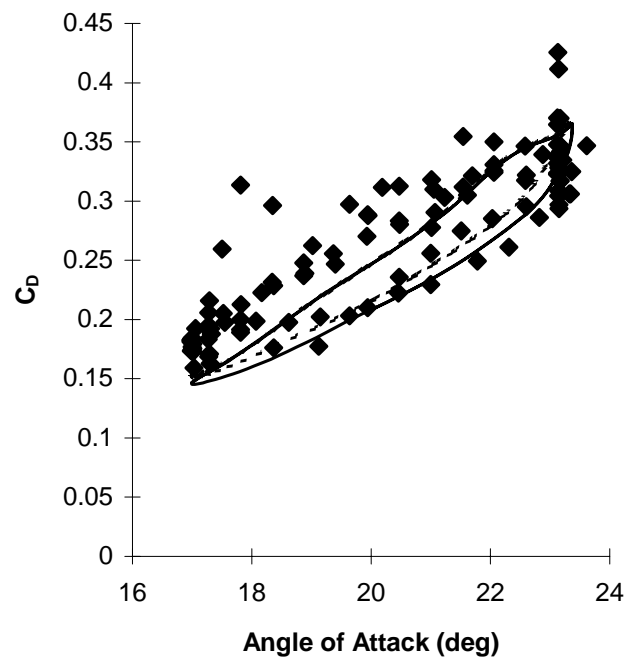


Figure 18: NACA 4415 drag coefficient versus angle of attack. Conditions as given in Figure 17.

ber, and k is the reduced frequency, given by $k = \omega c / (2V)$, where c is the chord length, and V is the flow velocity. Included in the figures are the effects of the effective separation point shift. Figures 15 and 16 are comparisons for high amplitude of oscillation, while Figures 17 and 18 are comparisons for low amplitude oscillation. As can be seen in Figure 15, for the high amplitude oscillation, the shifting of the lookup location for the effective separation point increases accuracy by delaying flow reattachment. There is little effect on the drag. However for the low amplitude case shown in Figure 17, the shifting overestimates the loss of lift for decreasing angle of attack. Thus for the low amplitude oscillation case, the model without shifting the effective separation lookup point more accurately reproduces the observed hysteresis. Also the drag prediction is somewhat improved. During code run time one does not know before hand what the amplitude of oscillation will be, for this reason it is more accurate to eliminate the shifting from the model used in AeroDyn. Also, at very low amplitudes of oscillation the shifting resulted in discontinuities in the lift and drag predictions. These discontinuities result in convergence problems for the ADAMS integrator.

An alternative method to shifting the point of lookup for decreasing angles of attack, is to increase the time constant associated with the motion of the effective separation point for decreasing angles of attack. Increasing the time constant of the first order lag by a factor of 1.5 for decreasing angles of attack produces nearly the same effect as shifting for the high amplitude oscillation without discontinuities or over-estimation of lift loss for low amplitude oscillation. This is the method currently used in AeroDyn, and is illustrated in Figures 19 through 22.

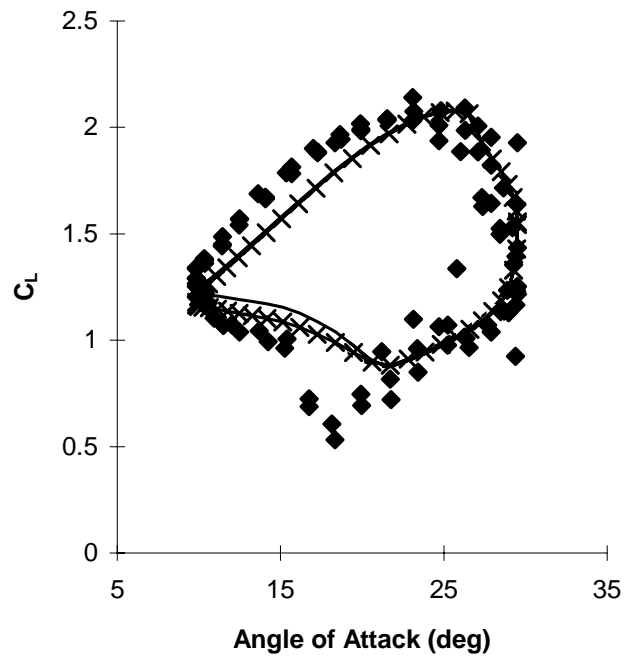


Figure 19: NACA 4415 lift coefficient versus angle of attack. High amplitude oscillation. $\alpha=19.7+9.8\sin(\omega t)$, $k=0.096$, $M=0.1$ Shown are the effects of separation point time constant increase for decreasing angle of attack.

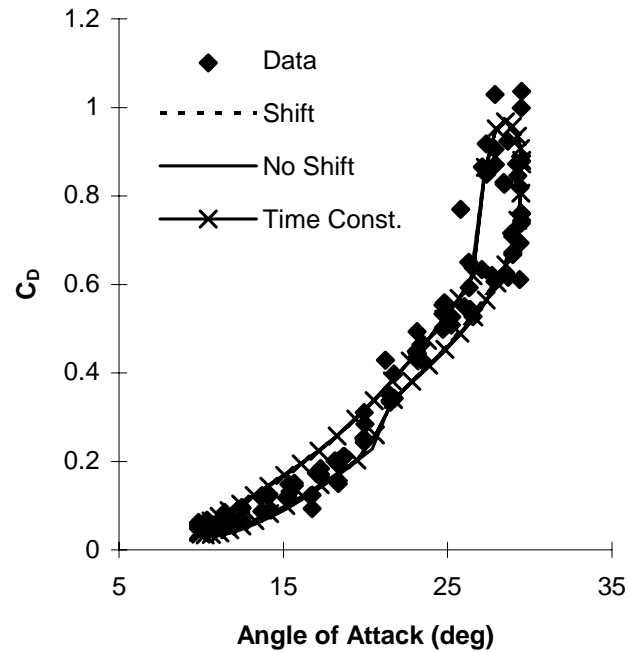


Figure 20: NACA 4415 drag coefficient versus angle of attack. Conditions as given in Figure 19.

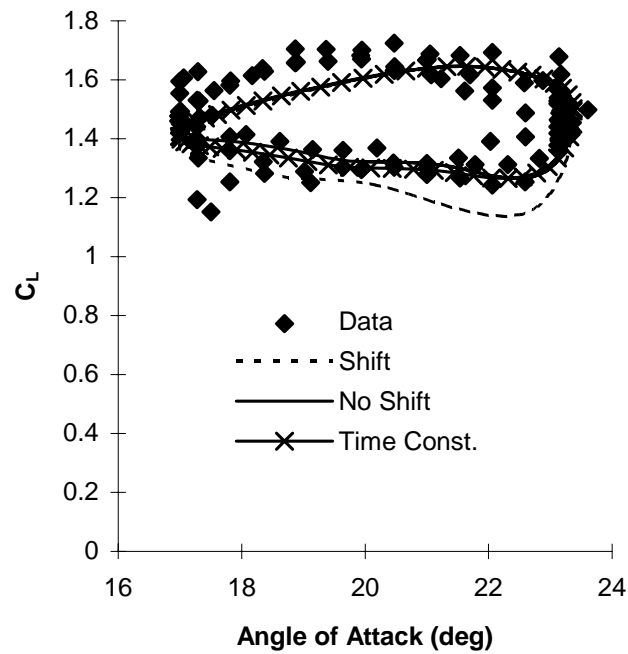


Figure 21: NACA 4415 lift coefficient versus angle of attack. Low amplitude oscillation.
 $\alpha=20.2+3.2\sin(\omega t)$, $k=0.087$, $M=0.1$ Shown are the effects of separation point time constant increase for decreasing angle of attack.

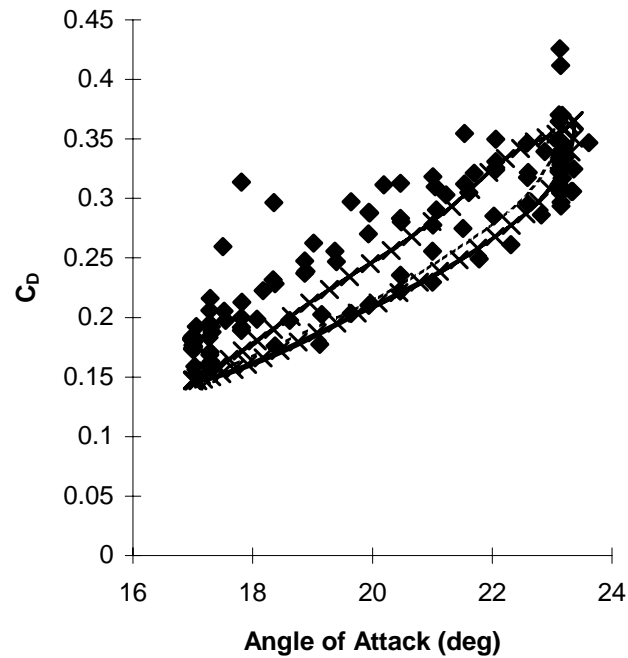


Figure 22: NACA 4415 drag coefficient versus angle of attack. Conditions as given in Figure 21.

NACA 4415 Airfoil

Figures 23 through 34 are comparisons between predicted and measured C_L and C_D hysteresis curves for a NACA 4415. In these figures comparisons with data were made for mean angles of attack of 14° and 20° , with an amplitude of oscillation of 10° . For each mean value of angle of attack comparisons were made for three reduced frequencies. This allows observation of the effects of reduced frequency on the aerodynamic coefficient hysteresis, and the ability of the model to represent the aerodynamic force coefficients for a range of reduced frequencies. In general the model accurately represents the hysteresis in C_L and C_D over the range of reduced frequencies tested.

For this airfoil section static drag data were not available for angles of attack above 12° . The values used in the predictions were estimated based on the unsteady data, and the Kirchhoff equation.

Multiple lines occur in the predictions since the measured angle of attack from the data was used as input to the Beddoes subroutines. The subroutines, written in FORTRAN, are given in the program DYNSTL in Appendix B. The measured angle of attack does not follow an exact sine wave, and the measurements are somewhat sparse resulting in the multiple prediction lines.

At 14° mean angle of attack, the aerodynamic coefficient predictions are quite good for the low reduced frequency case as shown in Figures 23 and 24. The predicted C_L does stall more rapidly and deeply than observed in the data. It appears from the data that the vortex builds more slowly, then remains near the airfoil until the angle of attack begins to decrease. The C_D for this case is well represented. For the two higher reduced frequencies, Figures 25-28, consistent errors in the predicted C_L occur in the separated

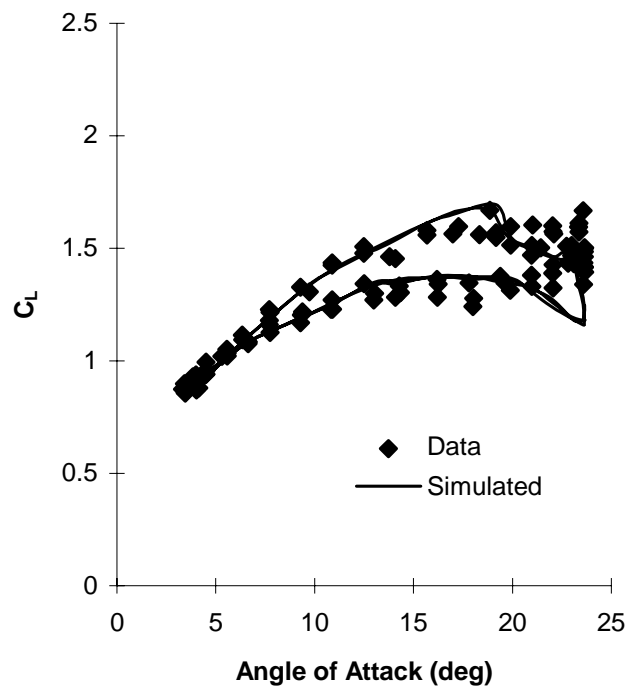


Figure 23: NACA 4415 lift coefficient versus angle of attack. $\alpha=14+10\sin\omega t$, $k=0.029$, $M=0.09$

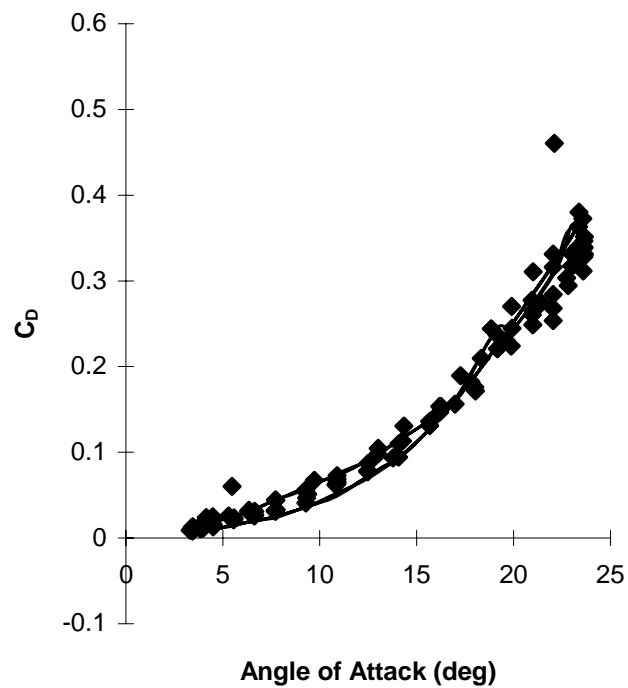


Figure 24: NACA 4415 drag coefficient versus angle of attack. Conditions as given in Figure 23.

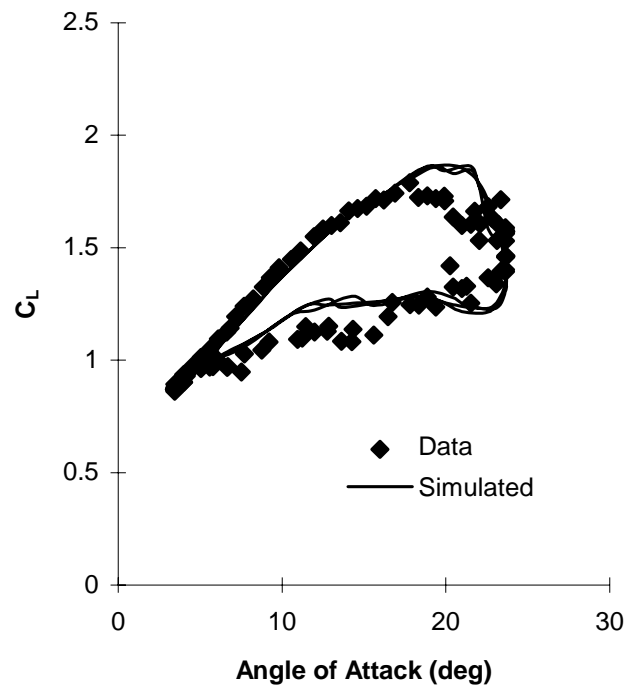


Figure 25: NACA 4415 lift coefficient versus angle of attack. $\alpha=14+10\sin\omega t$, $k=0.055$, $M=0.09$

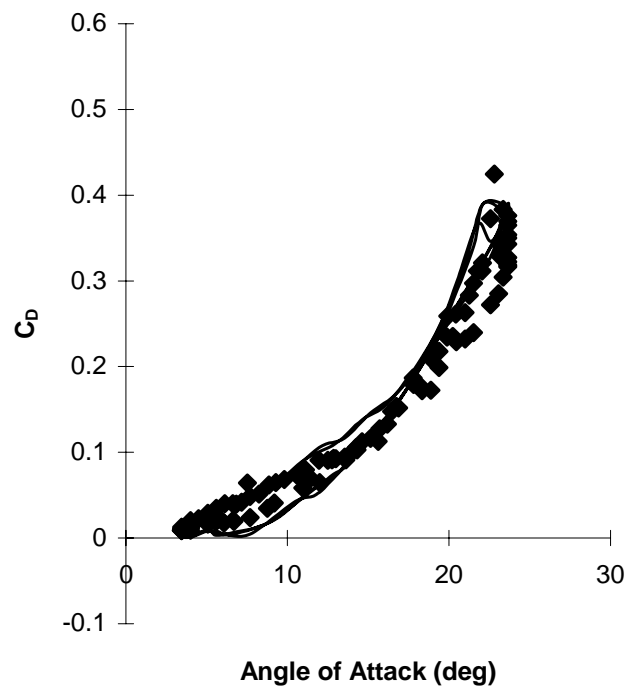


Figure 26: NACA 4415 drag coefficient versus angle of attack. Conditions as given in Figure 25.

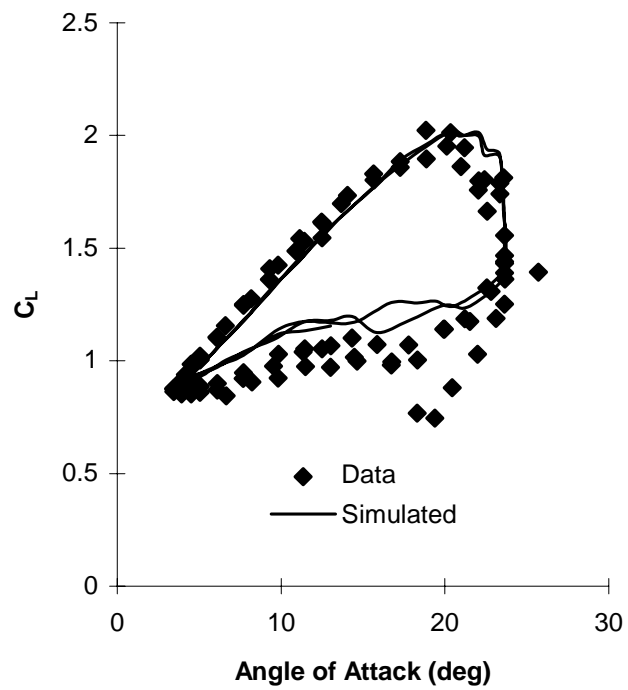


Figure 27: NACA 4415 lift coefficient versus angle of attack. $\alpha=14+10\sin\omega t$, $k=0.086$, $M=0.09$

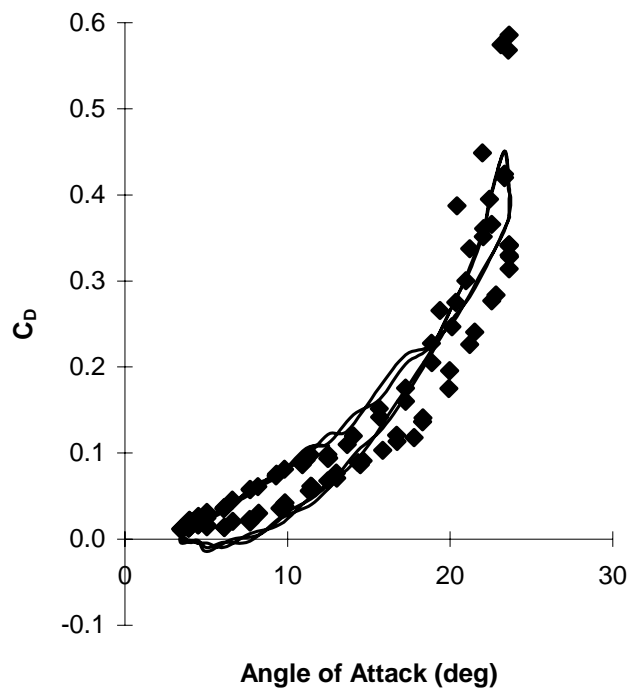


Figure 28: NACA 4415 drag coefficient versus angle of attack. Conditions as given in Figure 27.

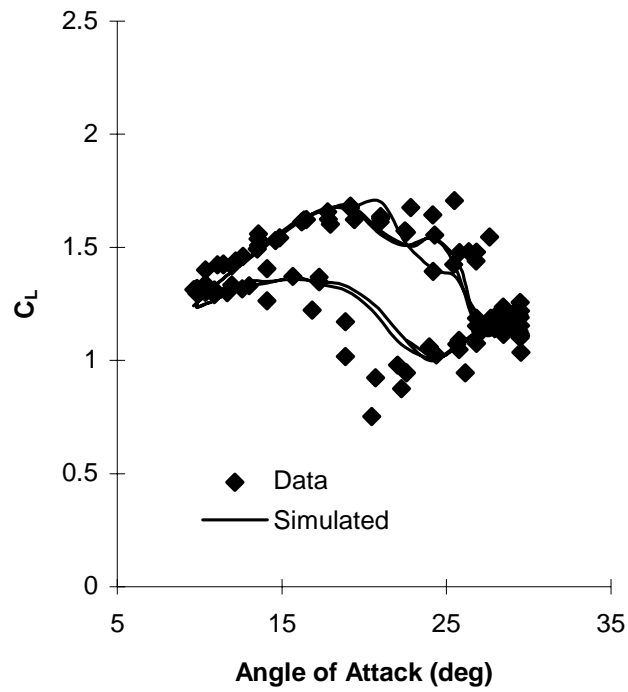


Figure 29: NACA 4415 lift coefficient versus angle of attack. $\alpha=20+10\sin\omega t$, $k=0.031$, $M=0.08$

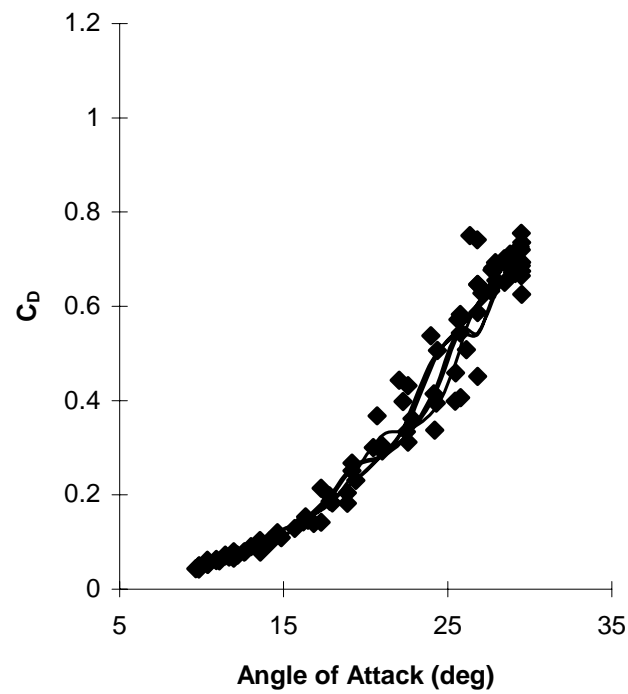


Figure 30: NACA 4415 drag coefficient versus angle of attack. Conditions as given in Figure 29.

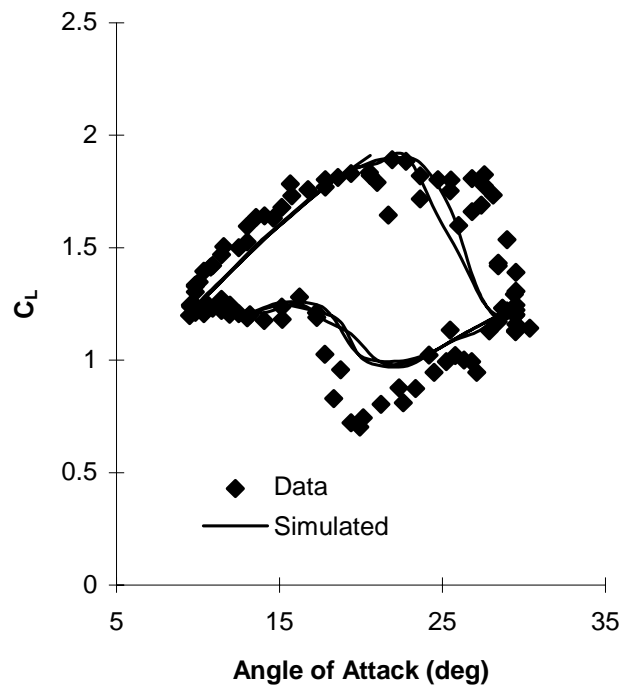


Figure 31: NACA 4415 lift coefficient versus angle of attack. $\alpha=20+10\sin\omega t$, $k=0.064$, $M=0.08$

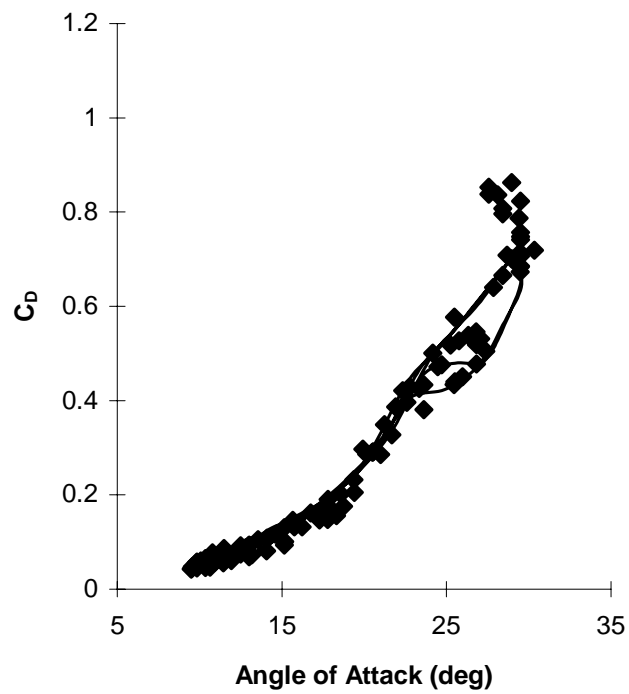


Figure 32: NACA 4415 drag coefficient versus angle of attack. Conditions as given in Figure 31.

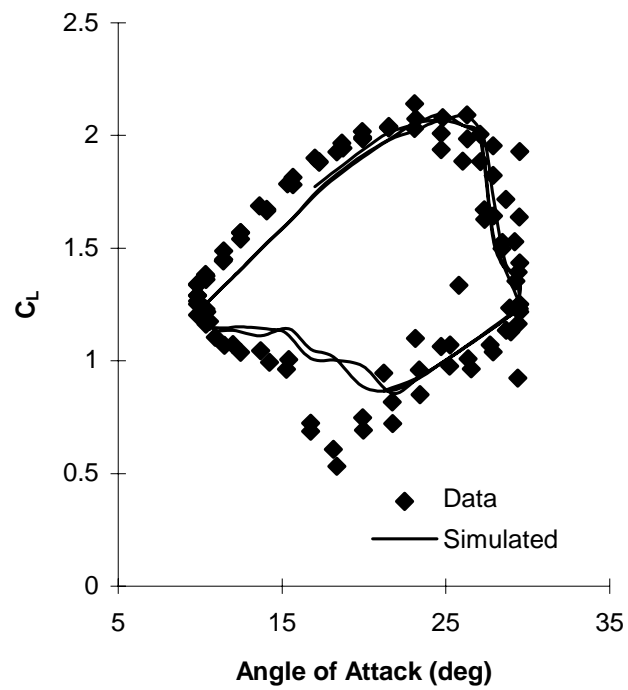


Figure 33: NACA 4415 lift coefficient versus angle of attack. $\alpha=20+10\sin\omega t$, $k=0.096$, $M=0.08$

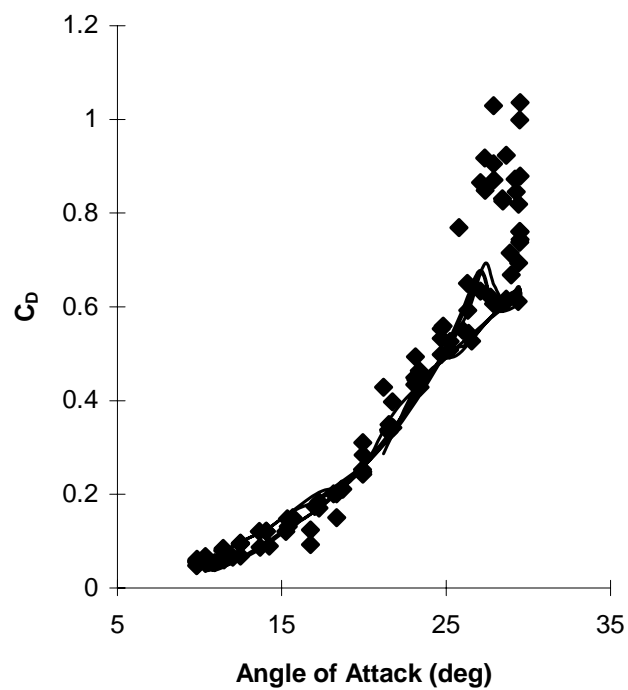


Figure 34: NACA 4415 drag coefficient versus angle of attack. Conditions as given in Figure 33.

flow region of the hysteresis. For these cases the model predicts that the flow is more attached than observed in the test data. This results in an overprediction of C_L for the lower region of the hysteresis. Also the vortex lift contribution is overestimated, or the vortex is not swept off the airfoil as early as observed in the data, producing the overestimation of C_L prior to stall. The C_D for these cases is well represented for the lower region, but at times lacks the width of the hysteresis for the upper region.

At 20° mean angle of attack, Figures 29-34, the sharp corners and the minimum C_L in the separated flow region are not predicted. In the data the flow remains fully separated for a time after stall, causing the sharp corners and minimum C_L . It then quickly reattaches as the angle of attack further decreases. For the model, the flow slowly reattaches, and therefore misses the minimum value. However, the general shape of the hysteresis is well represented. The vortex contribution seems to be governed by somewhat different dynamics. The vortex lift does not build then decay as predicted by the model. It seems to build then stay nearly constant in strength for a short time before being swept off of the airfoil. The C_D is accurately predicted for the low reduced frequency case, Figure 30, but misses the maximum value for the higher reduced frequency cases, Figures 32 and 34.

For the high reduced frequency, high amplitude of oscillation cases, the maximum value and width of the loops in the upper section of the C_D hysteresis are not obtained due to the predicted C_C not stalling as rapidly as observed in the data. Predicted and measured C_C showing this effect are given in Figure 35. Figure 36 illustrates the chronology of events resulting in the large value of C_D and the width of the hysteresis for the

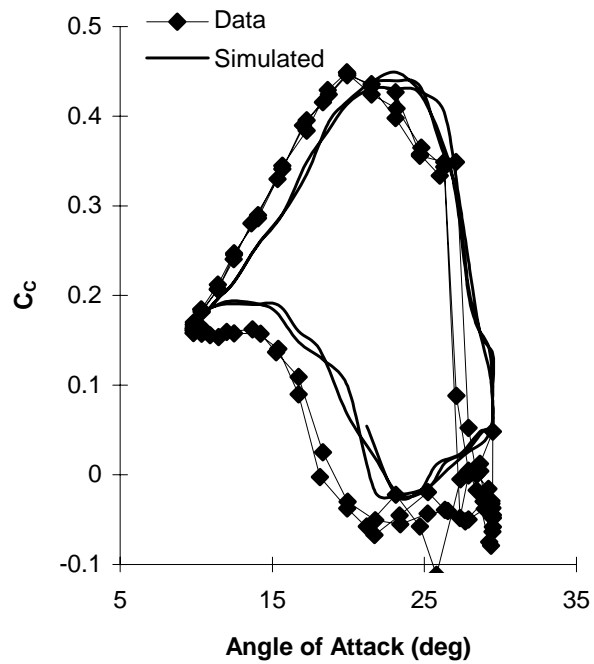


Figure 35: Chordwise force coefficient versus angle of attack. Conditions as given in Figure 33. Simulated hysteresis does not stall as rapid as measured values.

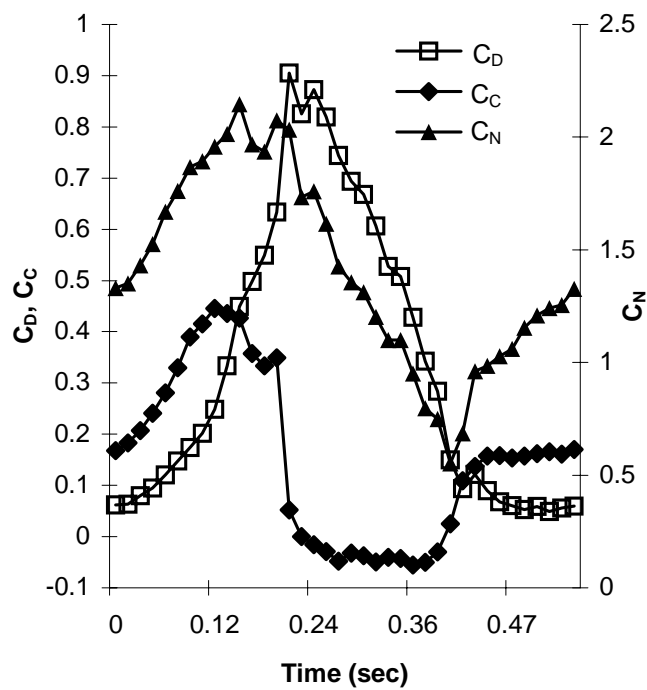


Figure 36: Chronology of measured aerodynamic coefficients. Conditions as given in Figure 33.

upper region. A description of the events is as follows: As C_N reaches its maximum value and begins to stall C_C stalls very rapidly to near zero. The rapid stall of C_C results in a rapid increase in C_D to the maximum value. The C_N then stalls to separated flow values, with a similar reduction of C_D , completing the hysteresis in the upper region.

Figures 37 through 42 are for lower amplitude of oscillation. The amplitude of oscillation for these cases is 3.5° , with mean angles of attack of 8° and 20° . For these cases the hysteresis in both C_L and C_D are well represented.

NREL S809 Airfoil

Figures 43 through 60 are comparisons between predicted and measured C_L and C_D hysteresis curves for an NREL S809. Comparisons with data were made for mean angles of attack of 20° , 14° , and 8° , with an amplitude of oscillation of 10° . For each mean value of angle of attack comparisons were made for three reduced frequencies. Multiple lines occur for the same reasons addressed in the previous section.

Again the model quite accurately represents the hysteresis in C_L over the range of reduced frequencies. One difference between the predictions and data for this airfoil occurs due to a very strong secondary vortex which is observed in the data for the 20° and 14° mean angle of attack cases. The model is capable of predicting and does predict secondary vortices; however the strength of the secondary vortices is much less than that observed in the data. Another possibility is that the large increase in lift is not due to a secondary vortex, but due to the primary vortex becoming organized and greatly increasing in strength before being swept off of the airfoil. Similar events, but of less magnitude, seem to occur in other published data (Carr, 1988).

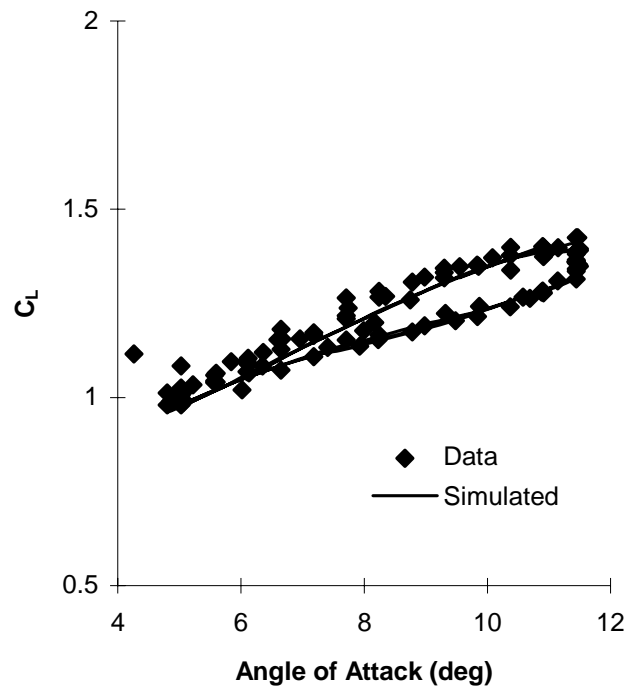


Figure 37: NACA 4415 lift coefficient versus angle of attack. $\alpha=8+3.5\sin\omega t$, $k=0.059$, $M=0.09$

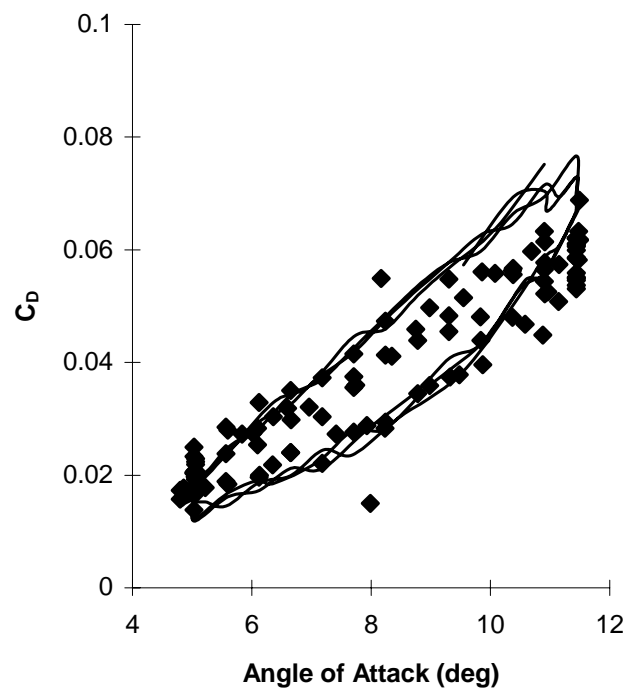


Figure 38: NACA 4415 drag coefficient versus angle of attack. Conditions as given in Figure 37.

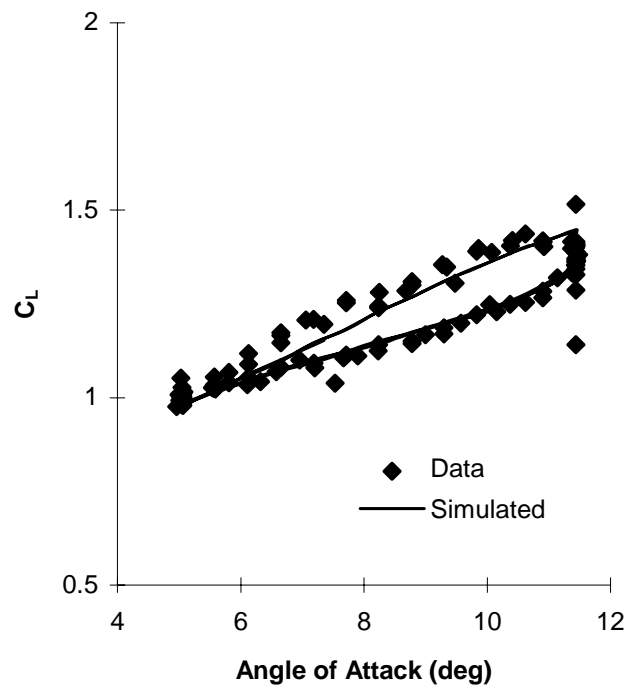


Figure 39: NACA 4415 lift coefficient versus angle of attack. $\alpha=8+3.5\sin\omega t$, $k=0.089$, $M=0.09$

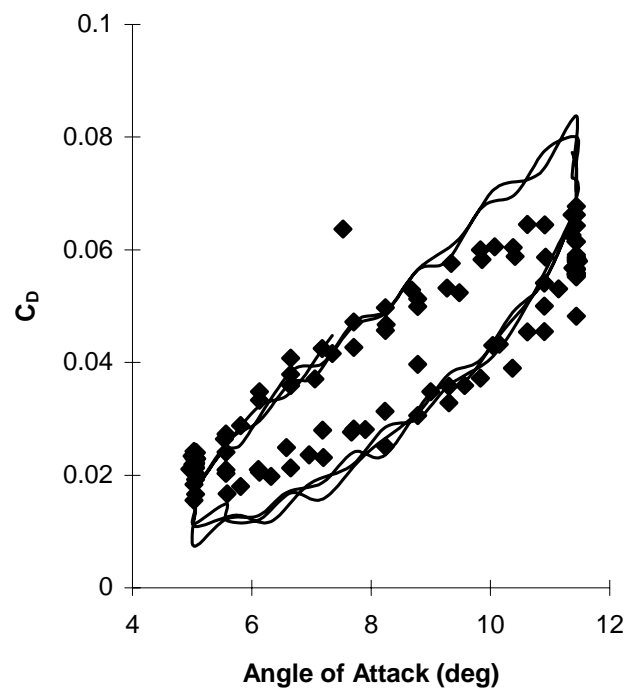


Figure 40: NACA 4415 drag coefficient versus angle of attack. Conditions as given in Figure 39.

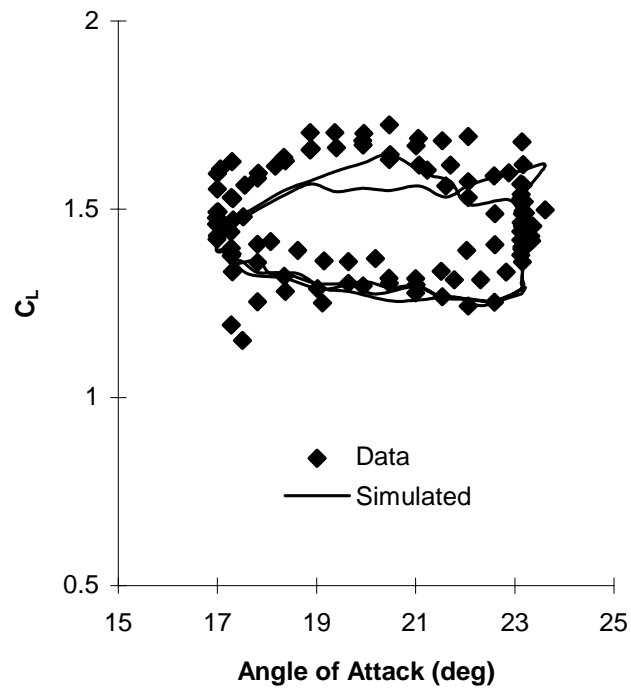


Figure 41: NACA 4415 lift coefficient versus angle of attack. $\alpha=20+3.5\sin\omega t$, $k=0.087$, $M=0.09$

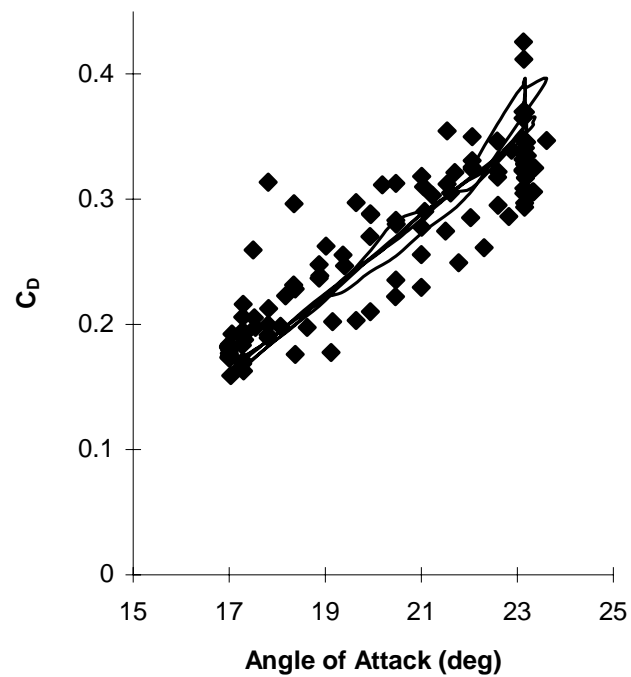


Figure 42: NACA 4415 drag coefficient versus angle of attack. Conditions as given in Figure 41.

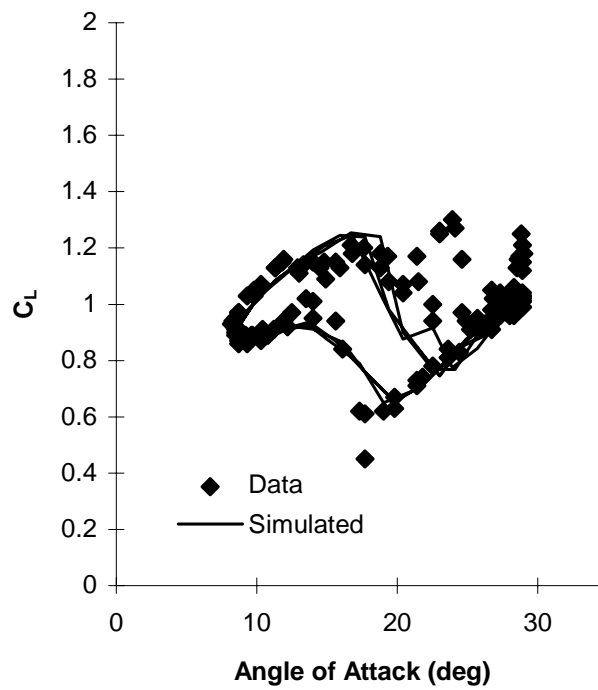


Figure 43: NREL S809 lift coefficient versus angle of attack. $\alpha=20+10\sin\omega t$, $k=0.025$, $M=0.1$

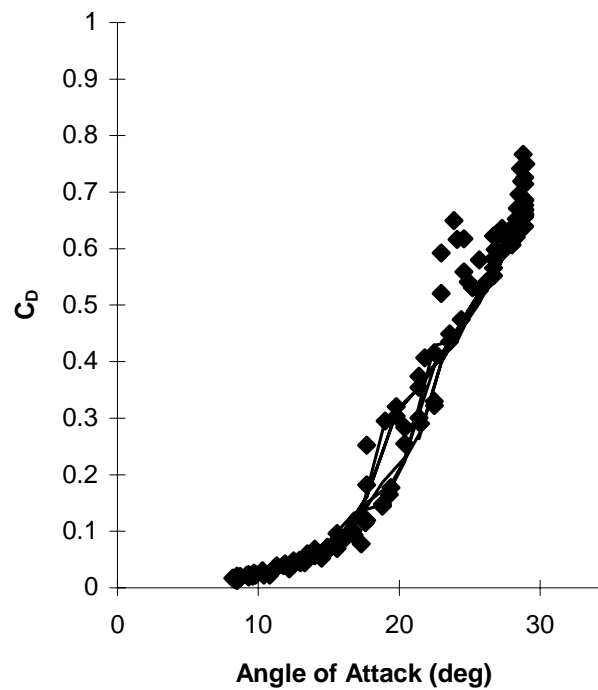


Figure 44: NREL S809 drag coefficient versus angle of attack. Conditions as given in Figure 43.

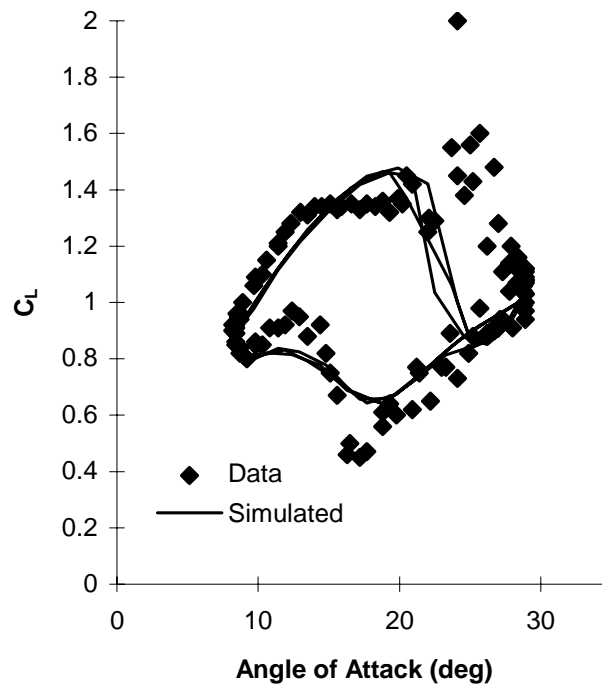


Figure 45: NREL S809 lift coefficient versus angle of attack. $\alpha=20+10\sin\omega t$, $k=0.051$, $M=0.1$

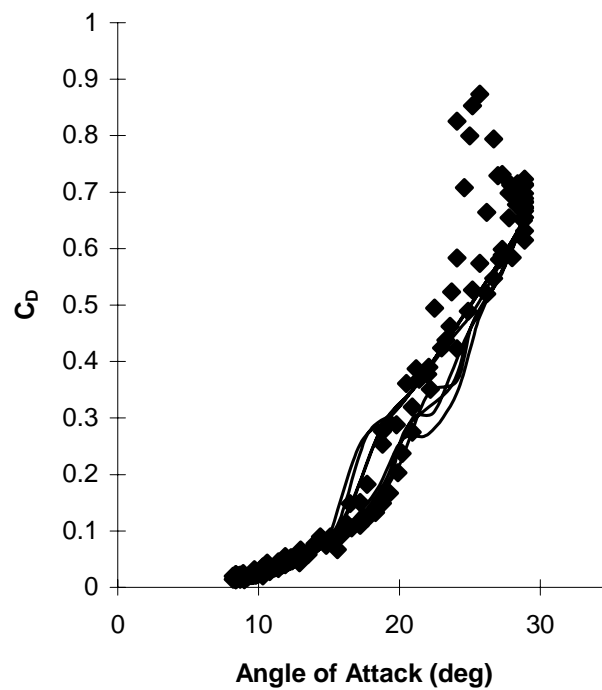


Figure 46: NREL S809 drag coefficient versus angle of attack. Conditions as given in Figure 45.

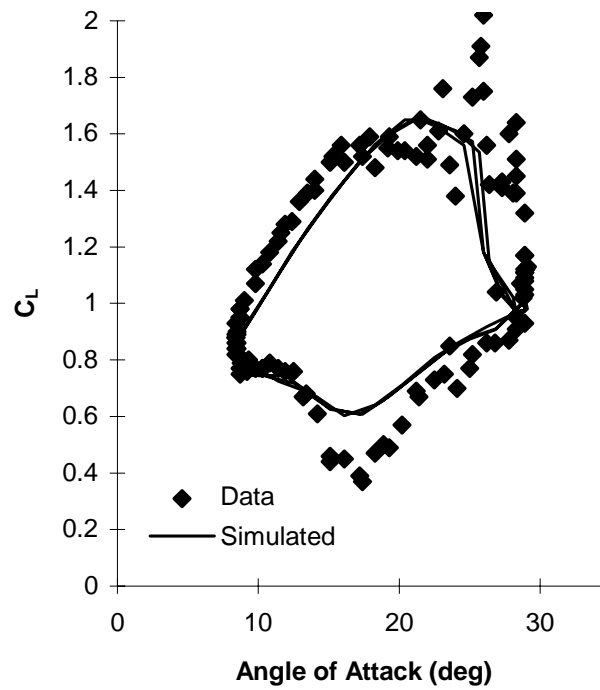


Figure 47: NREL S809 lift coefficient versus angle of attack. $\alpha=20+10\sin\omega t$, $k=0.078$, $M=0.1$

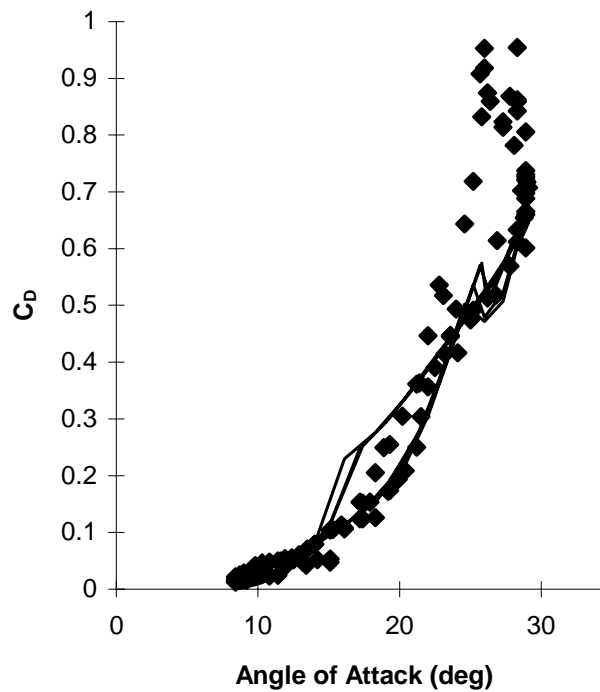


Figure 48: NREL S809 drag coefficient versus angle of attack. Conditions as given in Figure 47.

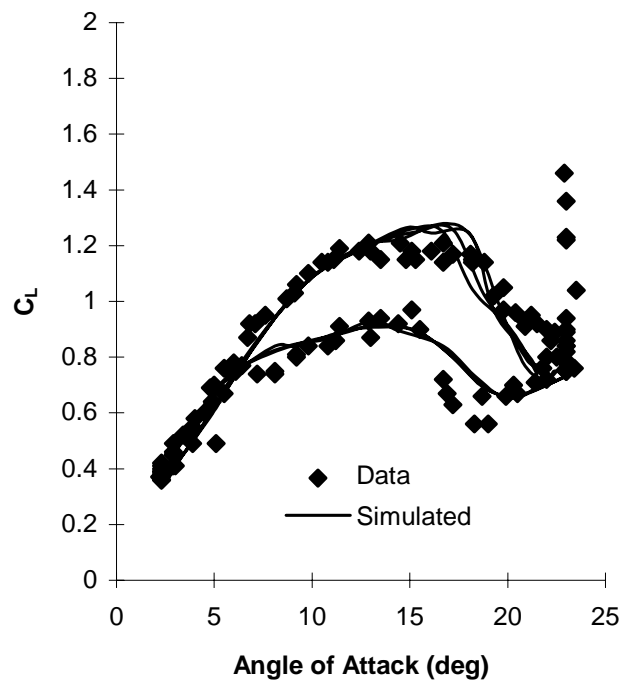


Figure 49: NREL S809 lift coefficient versus angle of attack. $\alpha=14+10\sin\omega t$, $k=0.026$, $M=0.1$

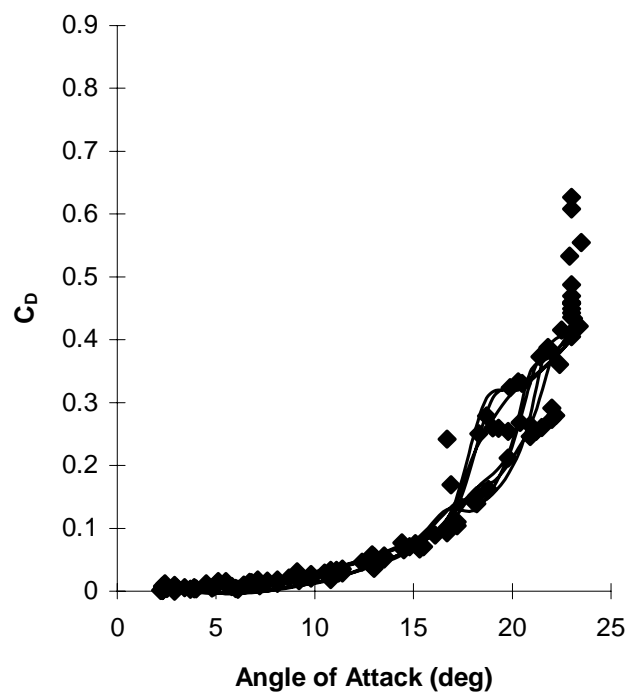


Figure 50: NREL S809 drag coefficient versus angle of attack. Conditions as given in Figure 49.

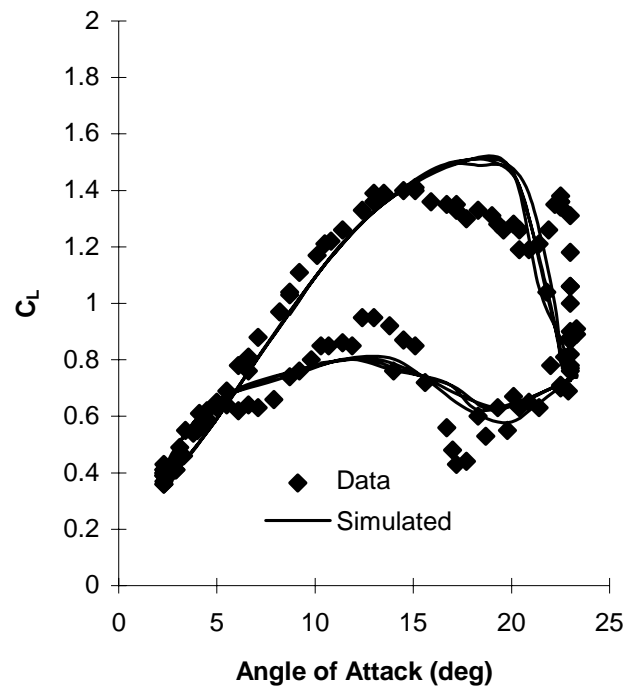


Figure 51: NREL S809 lift coefficient versus angle of attack. $\alpha=20+10\sin\omega t$, $k=0.053$, $M=0.1$

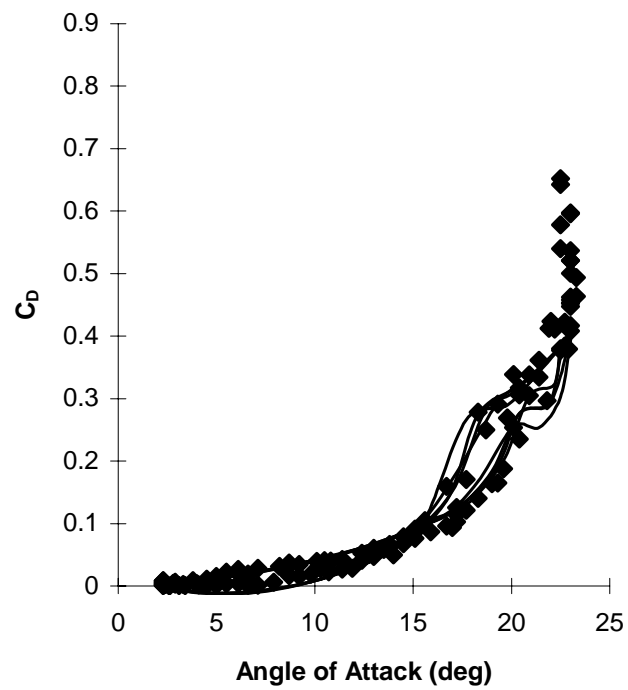


Figure 52: NREL S809 drag coefficient versus angle of attack. Conditions as given in Figure 51.

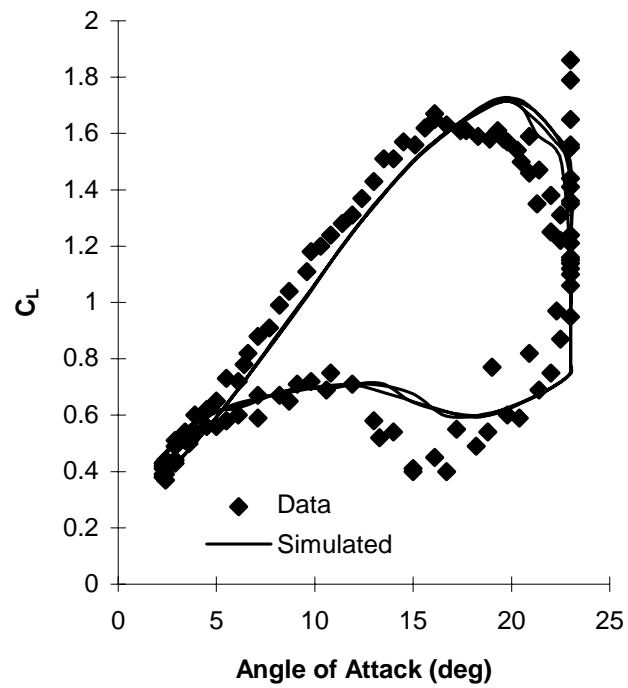


Figure 53: NREL S809 lift coefficient versus angle of attack. $\alpha=14+10\sin\omega t$, $k=0.080$, $M=0.1$

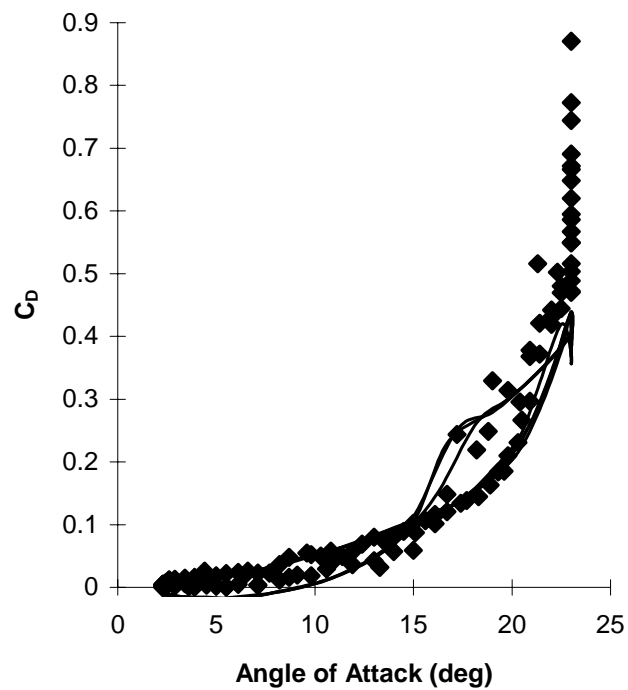


Figure 54: NREL S809 drag coefficient versus angle of attack. Conditions as given in Figure 53.

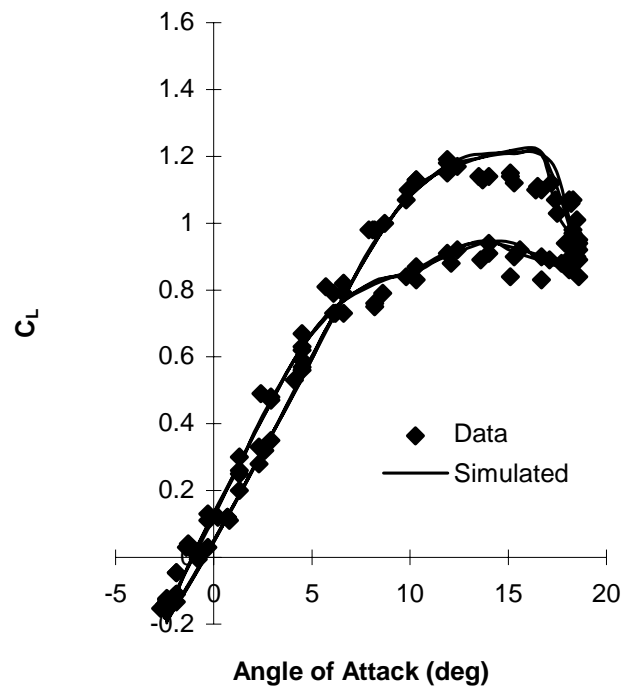


Figure 55: NREL S809 lift coefficient versus angle of attack. $\alpha=8+10\sin\omega t$, $k=0.026$, $M=0.1$

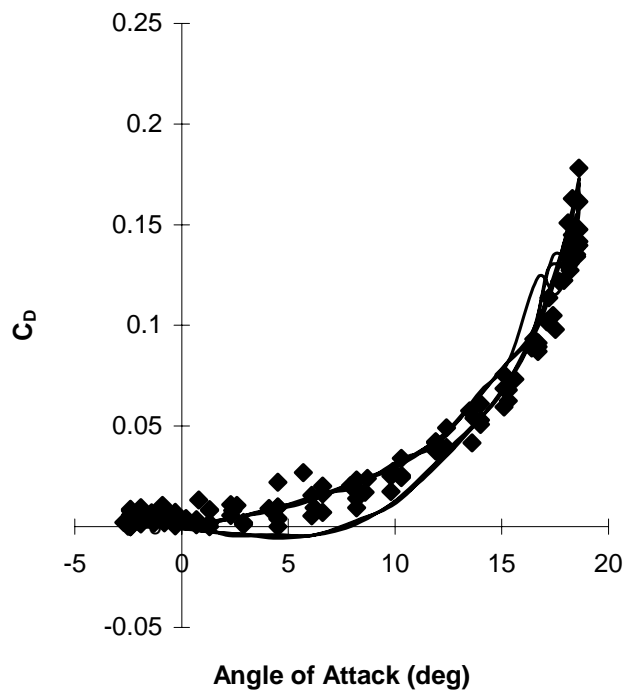


Figure 56: NREL S809 drag coefficient versus angle of attack. Conditions as given in Figure 55.

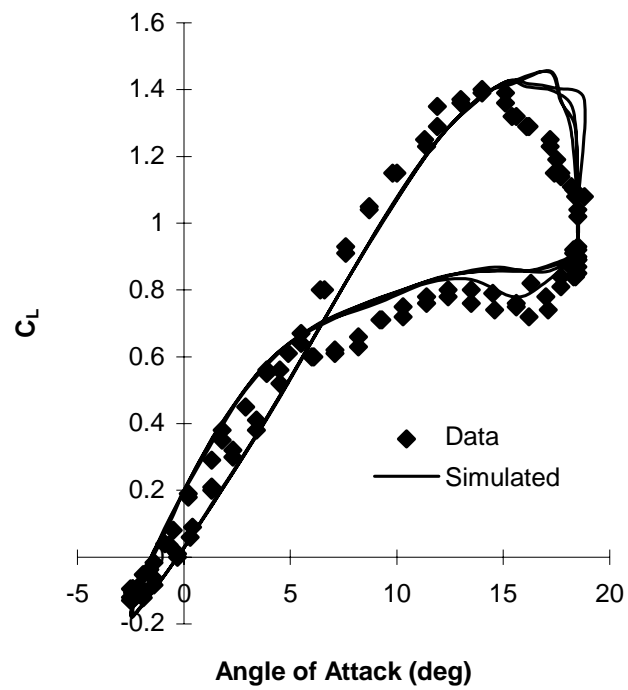


Figure 57: NREL S809 lift coefficient versus angle of attack. $\alpha=8+10\sin\omega t$, $k=0.053$, $M=0.1$

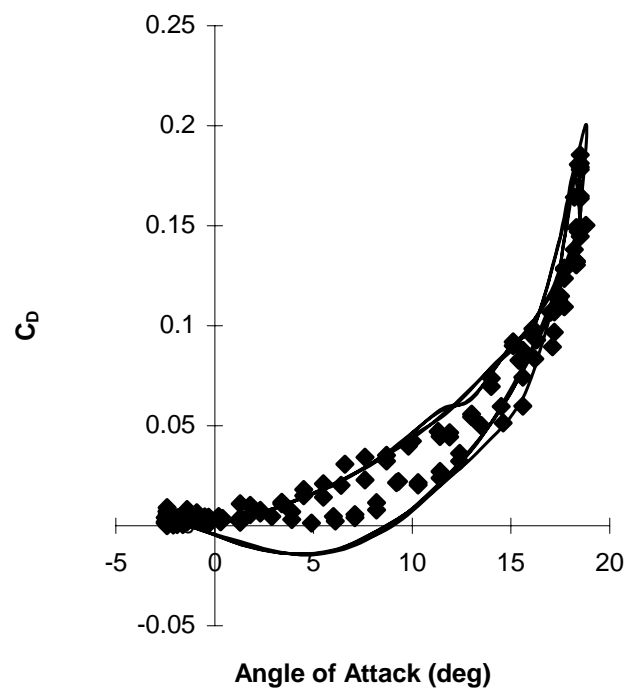


Figure 58: NREL S809 drag coefficient versus angle of attack. Conditions as given in Figure 57.

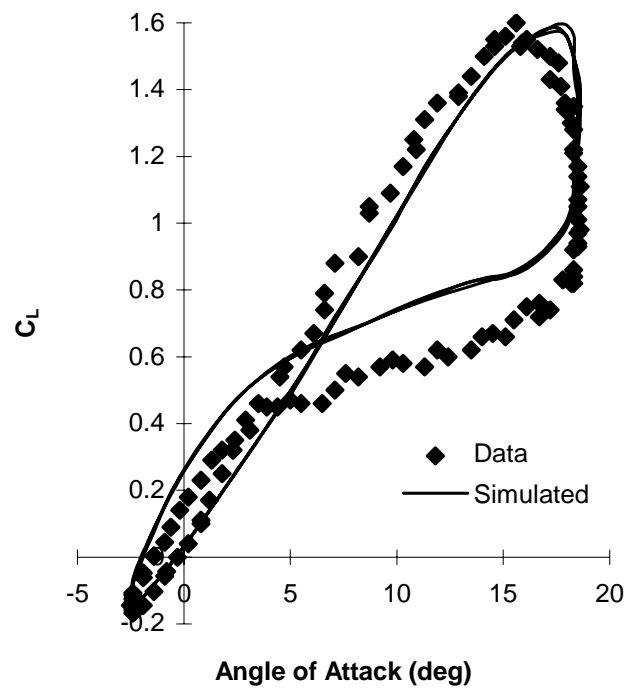


Figure 59: NREL S809 lift coefficient versus angle of attack. $\alpha=8+10\sin\omega t$, $k=0.077$, $M=0.1$

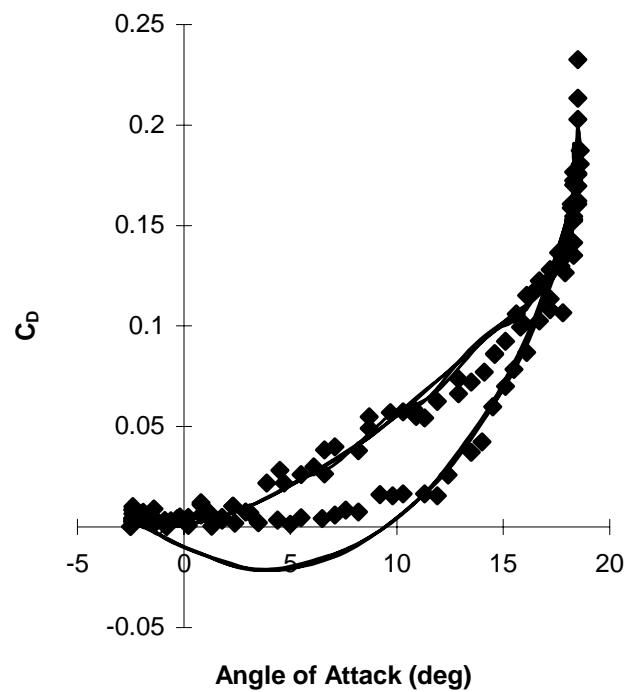


Figure 60: NREL S809 drag coefficient versus angle of attack. Conditions as given in Figure 59.

For this airfoil at 20° mean angle of attack, Figures 43 to 48, the model generally misses the sharp corners and minimum C_L in the separated flow region, similar to that observed for the NACA 4415. The C_D prediction for the two higher reduced frequencies, underestimates the maximum value and the width of the hysteresis in the upper region, again similar to the NACA 4415. For this airfoil C_c usually does not stall as rapidly as it does for the 4415, allowing the model predictions to follow more accurately. However, there are times when the measured C_c does stall faster than the model predicts resulting in under-prediction of the maximum C_D and width of the hysteresis for the upper section.

At 14° mean angle of attack, Figures 49 to 54, the predictions of C_L and C_D are very accurate for the low reduced frequency case. For the two higher reduced frequency cases the amount of vortex lift in the prediction of C_L is overestimated. Also the sharp corners and minimum value in the separated region are lacking in the prediction. The hysteresis in C_D is well represented. The maximum value in this case is missed due to the model not predicting the strong vortex which occurs near the maximum value of angle of attack.

For 8° mean angle of attack, Figures 55 to 60, the comparisons are good for the low reduced frequency case, Figures 55 and 56, but become worse as the reduced frequency increases. The simulated C_L for the highest reduced frequency case, Figure 59, falls below the data for increasing angle of attack, and above the data for decreasing angle of attack. Some of the error is due to the attached flow hysteresis loops being more open than observed in the data for this reduced frequency. Below 5° angle of attack the

prediction is almost entirely based on the attached flow response. The attached flow hysteresis in C_c is also more open, and the flow is predicted to be more attached than observed in the data for decreasing angles of attack. This results in C_c being slightly below the data for increasing angles of attack, and above the data for decreasing angles of attack. At low angles of attack C_c is nearly in the opposite direction of C_D . The overprediction of C_c for decreasing angles of attack results in the C_D prediction falling below the data upon flow reattachment, even becoming negative as shown in Figure 60. The hysteresis in C_c for this case is shown in Figure 61. The unsteady data do not lag behind the static data for decreasing angles of attack as the model predicts.

NASA LS(1)-0417 Airfoil

Figures 62 through 81 are comparisons between predicted and measured aerody-

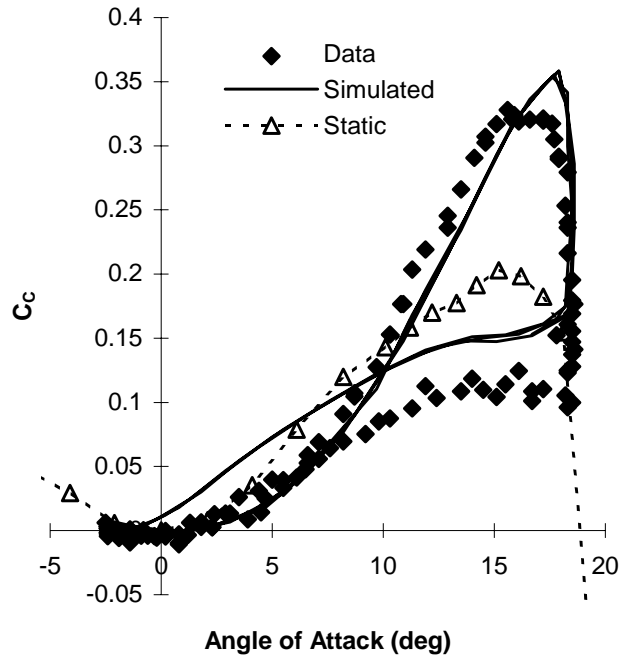


Figure 61: NREL S809 chordwise force coefficient versus angle of attack. Conditions as given in Figure 59.

dynamic coefficient hysteresis curves for a NASA LS(1)-0417. Again mean angles of attack

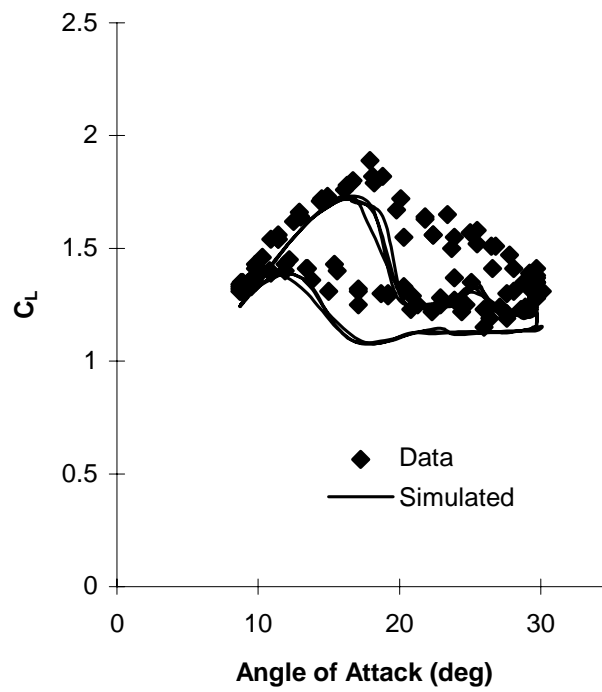


Figure 62: NASA LS(1)-0417 lift coefficient versus angle of attack. $\alpha=20+10\sin\omega t$, $k=0.027$, $M=0.1$

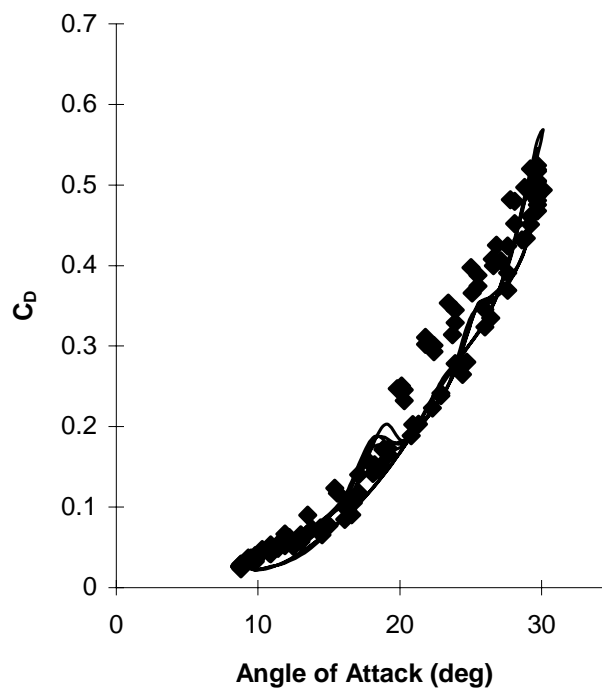


Figure 63: NASA LS(1)-0417 drag coefficient versus angle of attack. Conditions as given in Figure 62.

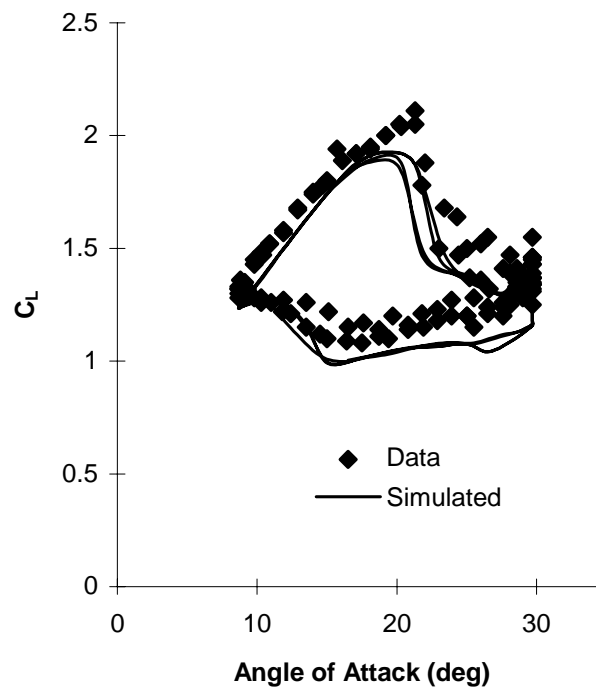


Figure 64: NASA LS(1)-0417 lift coefficient versus angle of attack. $\alpha=20+10\sin\omega t$, $k=0.055$, $M=0.1$

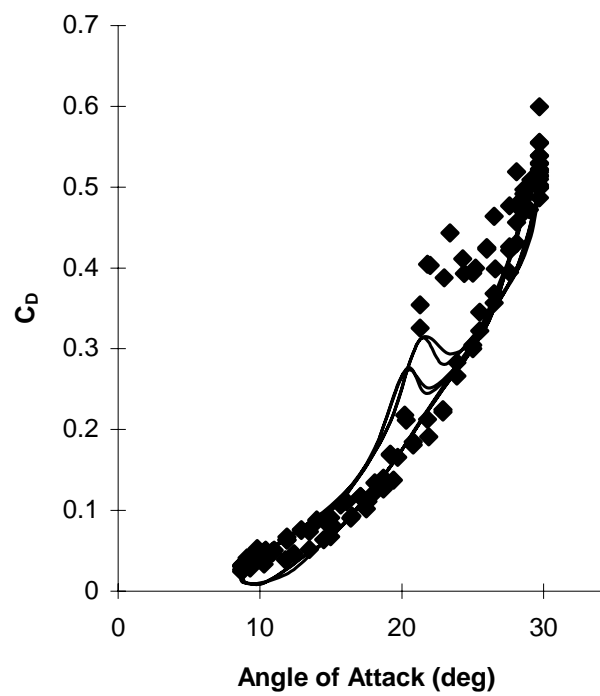


Figure 65: NASA LS(1)-0417 drag coefficient versus angle of attack. Conditions as given in Figure 64.

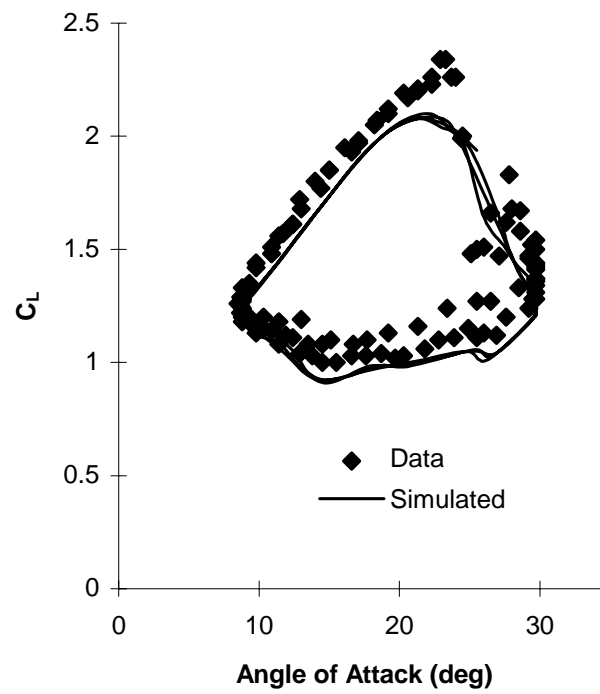


Figure 66: NASA LS(1)-0417 lift coefficient versus angle of attack. $\alpha=20+10\sin\omega t$, $k=0.081$, $M=0.1$

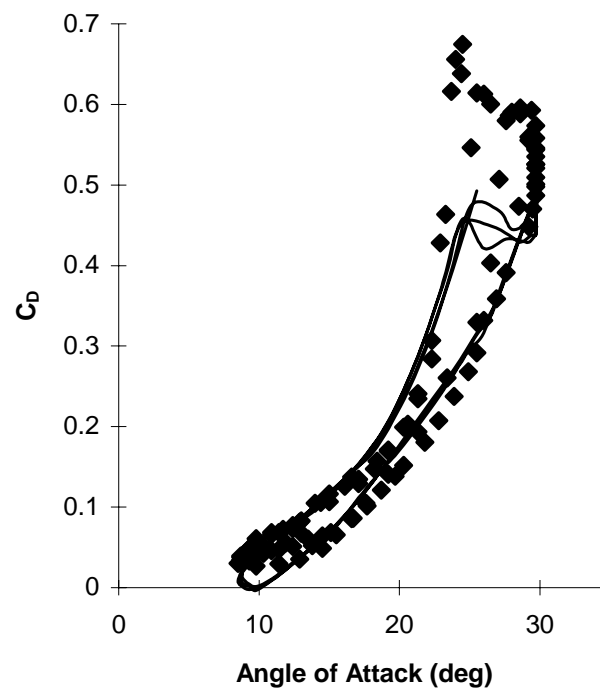


Figure 67: NASA LS(1)-0417 drag coefficient versus angle of attack. Conditions as given in Figure 66.

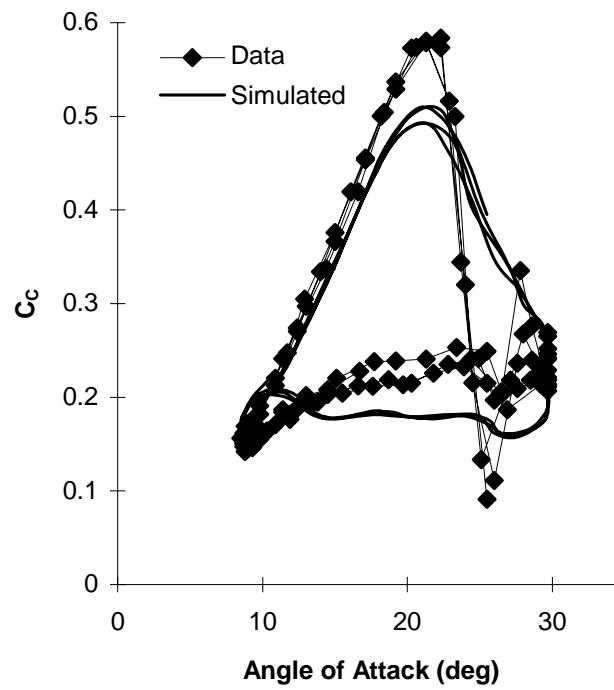


Figure 68: Chordwise force coefficient versus angle of attack. Conditions given in Figure 66. Predicted C_c does not stall as rapidly as the data.

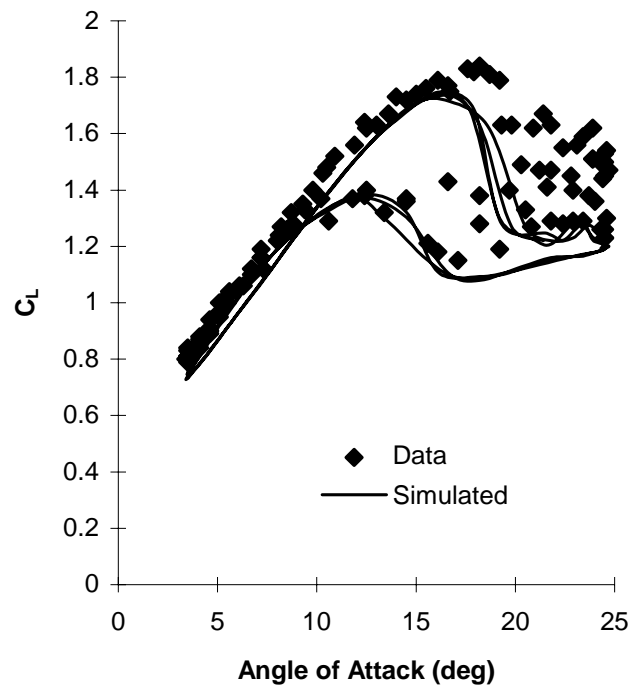


Figure 69: NASA LS(1)-0417 lift coefficient versus angle of attack. $\alpha=14+10\sin\omega t$, $k=0.026$, $M=0.1$

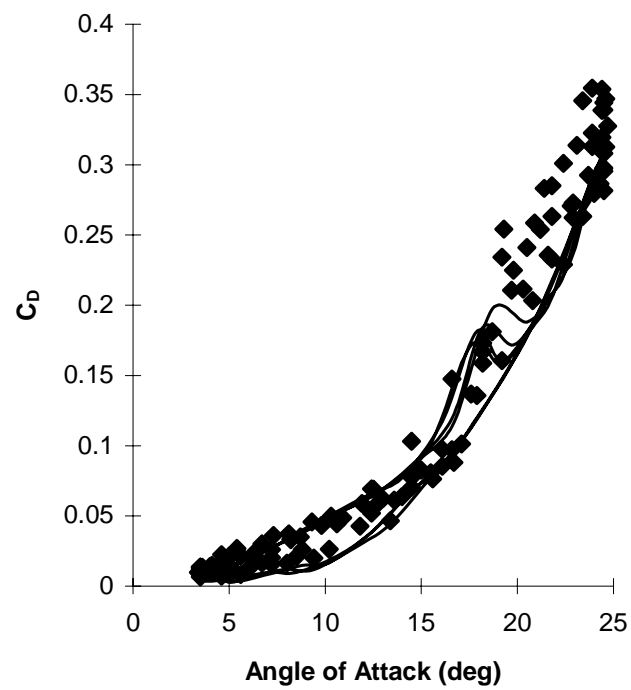


Figure 70: NASA LS(1)-0417 drag coefficient versus angle of attack. Conditions as given in Figure 69.

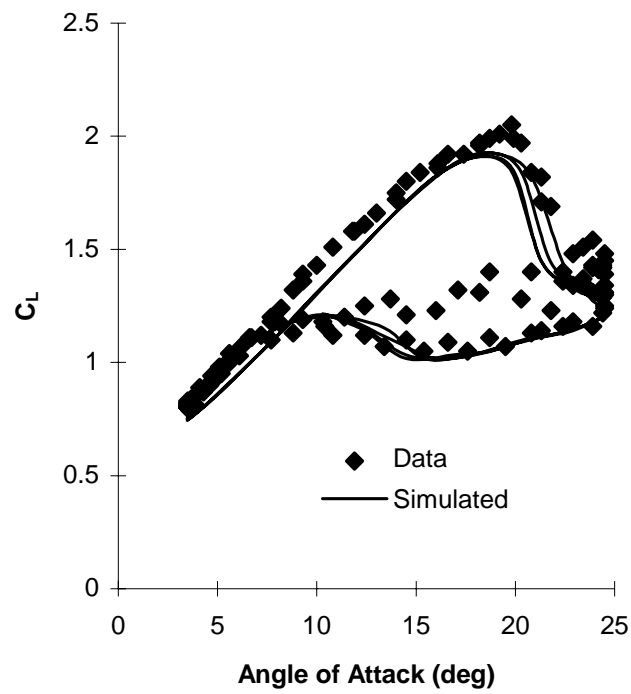


Figure 71: NASA LS(1)-0417 lift coefficient versus angle of attack. $\alpha=14+10\sin\omega t$, $k=0.052$, $M=0.1$

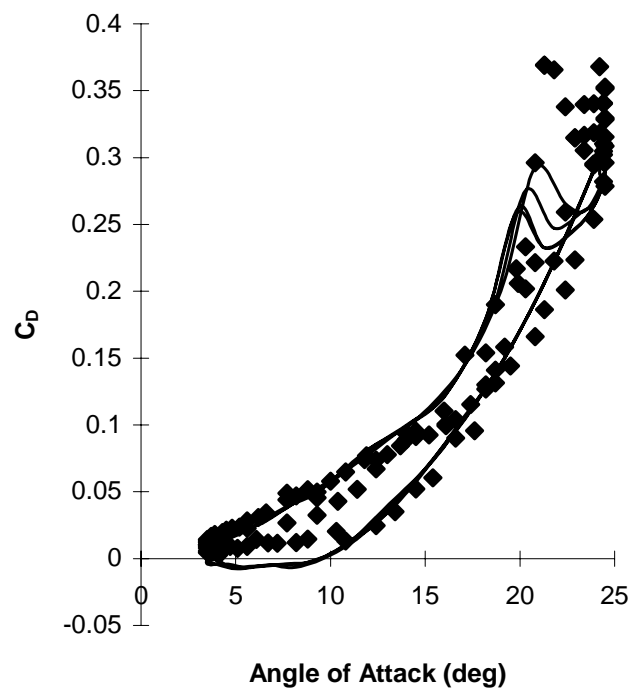


Figure 72: NASA LS(1)-0417 drag coefficient versus angle of attack. Conditions as given in Figure 71.

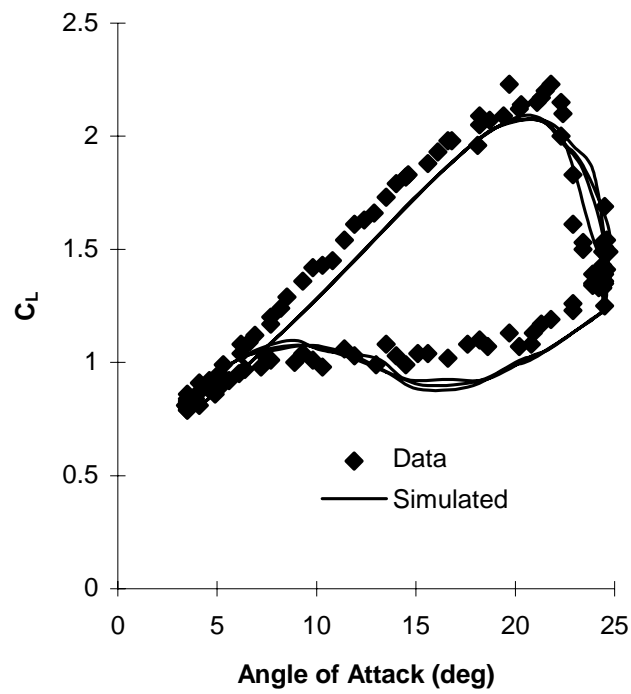


Figure 73: NASA LS(1)-0417 lift coefficient versus angle of attack. $\alpha=14+10\sin\omega t$, $k=0.079$, $M=0.1$

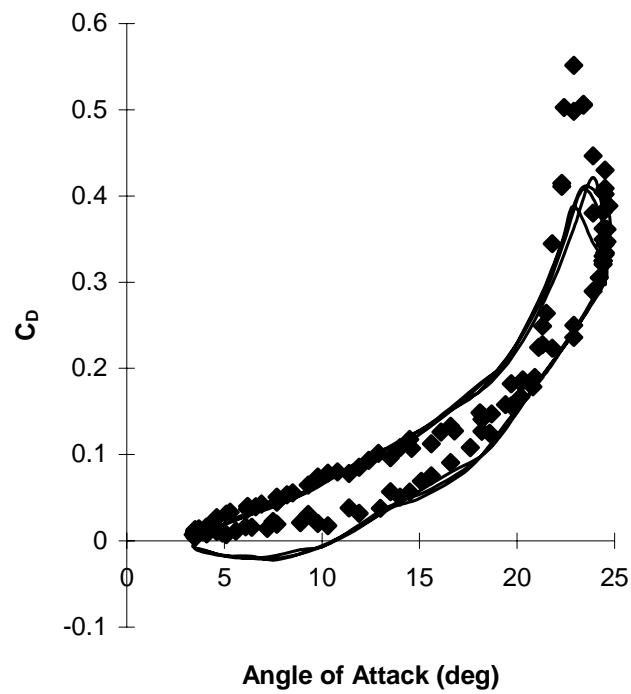


Figure 74: NASA LS(1)-0417 drag coefficient versus angle of attack. Conditions as given in Figure 73.

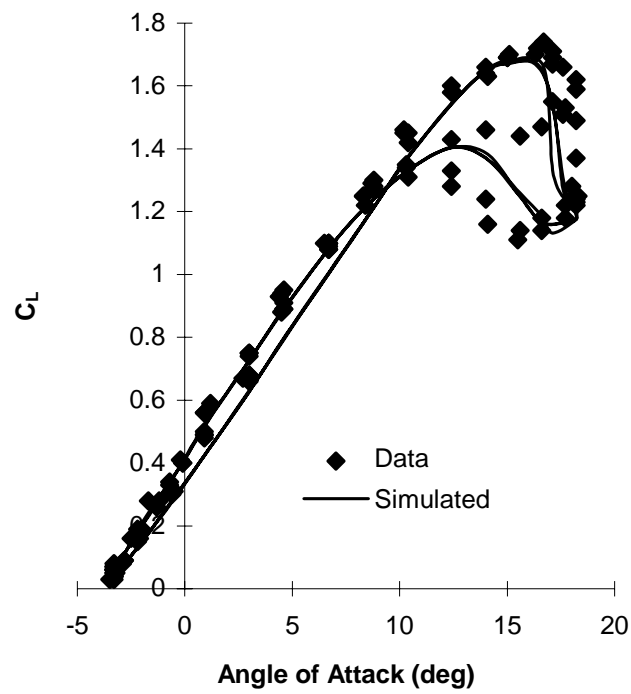


Figure 75: NASA LS(1)-0417 lift coefficient versus angle of attack. $\alpha=8+10\sin\omega t$, $k=0.026$, $M=0.1$

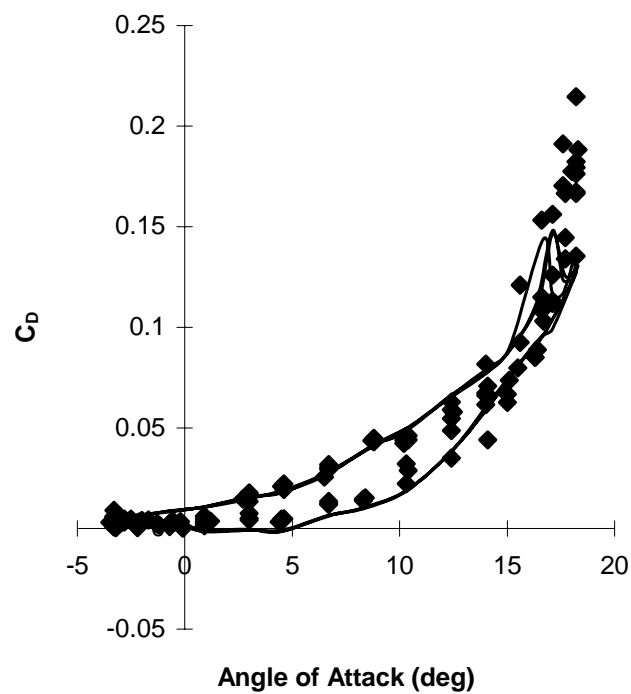


Figure 76: NASA LS(1)-0417 drag coefficient versus angle of attack. Conditions as given in Figure 75.

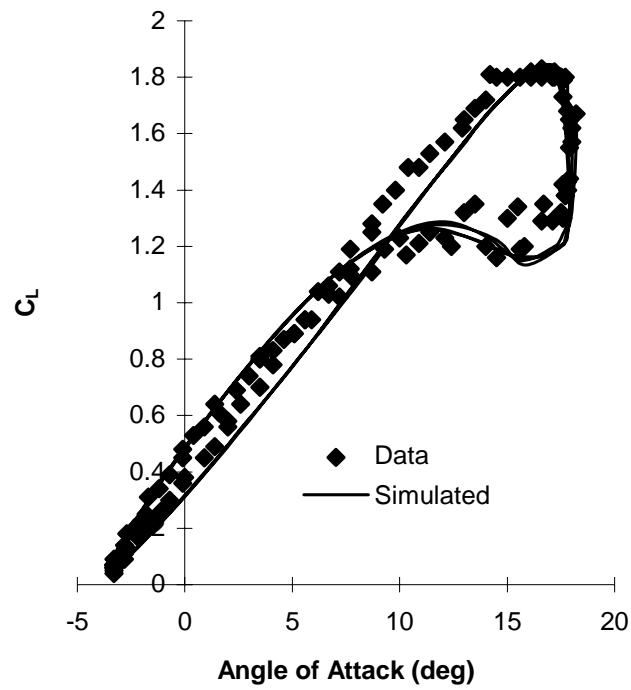


Figure 77: NASA LS(1)-0417 lift coefficient versus angle of attack. $\alpha=8+10\sin\omega t$, $k=0.052$, $M=0.1$

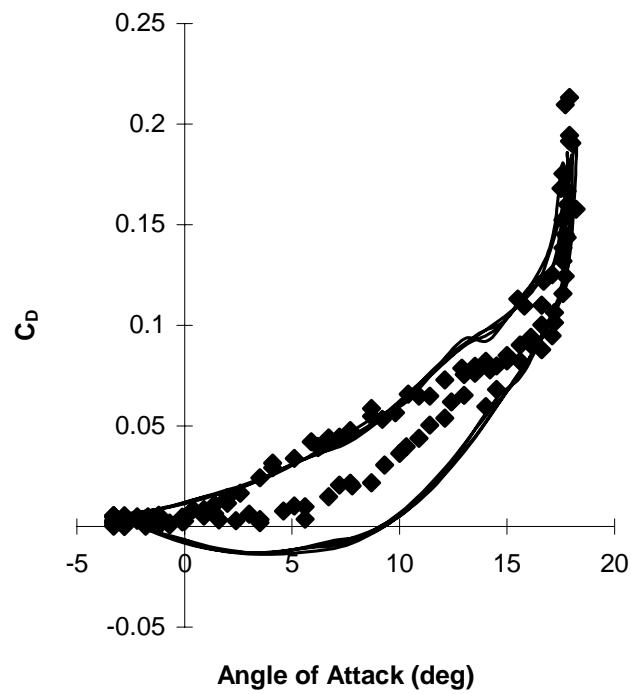


Figure 78: NASA LS(1)-0417 drag coefficient versus angle of attack. Conditions as given in Figure 77.

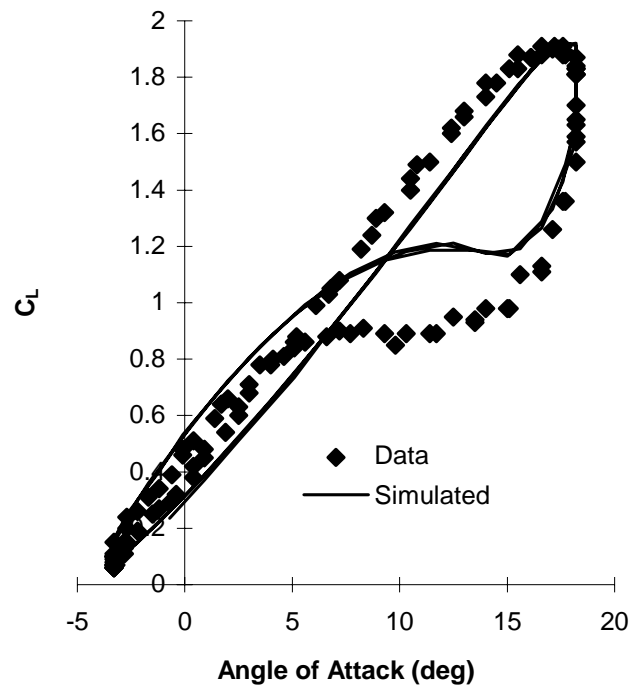


Figure 79: NASA LS(1)-0417 lift coefficient versus angle of attack. $\alpha=8+10\sin\omega t$, $k=0.082$, $M=0.1$

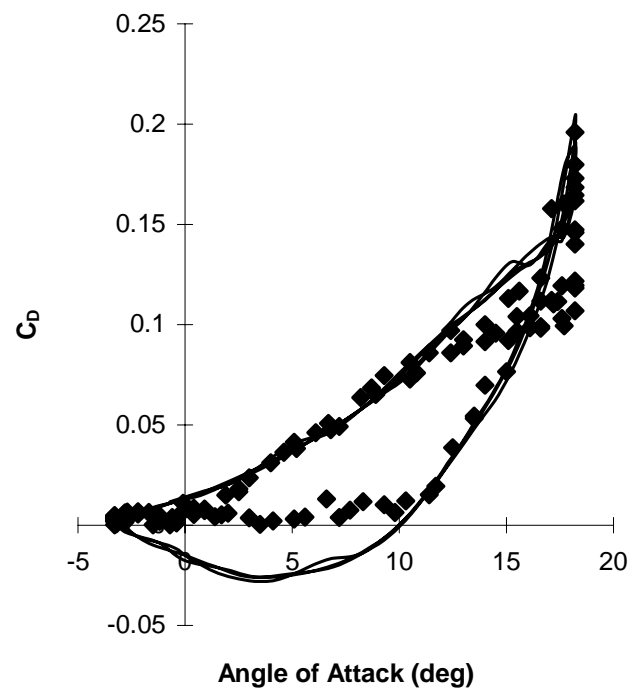


Figure 80: NASA LS(1)-0417 drag coefficient versus angle of attack. Conditions as given in Figure 79.

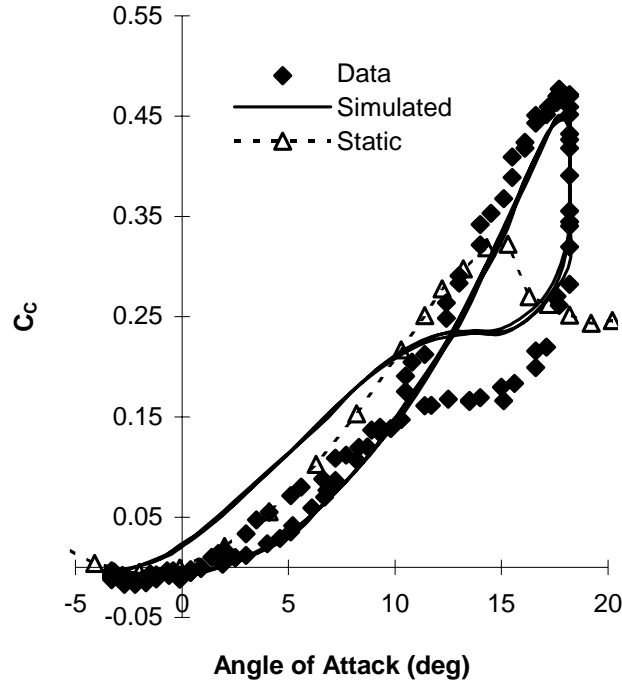


Figure 81: Chordwise force coefficient versus angle of attack. Conditions as given in Figure 79.

of 20° , 14° , and 8° , with an amplitude of oscillation of 10° , were used for the comparisons. For each mean value of angle of attack, three reduced frequencies were used in the comparisons. Multiple lines occur in the simulated curves as discussed previously.

At 20° mean angle of attack, for the lowest reduced frequency, Figure 62, the data does not stall as the model predicts. In the data the stall occurs gradually to the maximum angle of attack, whereas the model predicts a more rapid stall. The C_D is well represented for this case, as shown in Figure 63. For the higher reduced frequency cases, Figures 64 through 67, the hysteresis in C_L is quite well represented. In the data the C_L remains very linear until stall, then stalls very rapidly. The model predicts a more gradual stall, and rounds the peak values. However the minimum value in the separated flow region is represented for this airfoil. In the separated flow region the drop in C_L is not as

abrupt as seen for the two previous airfoils, allowing the model to follow more accurately. The maximum value of C_D is not predicted for the highest reduced frequency case, Figure 67, similar to that seen for the two previous airfoils for high mean angle of attack, high reduced frequency cases. This is again due to the C_C not stalling as rapidly as seen in the data, as illustrated in Figure 68. However the hysteresis in C_D are more open in the upper region than seen for the two previous airfoils.

At 14° mean angle of attack the hysteresis in C_L is well represented, as shown in Figures 69 through 74. At the lowest reduced frequency, Figure 69, again the model predicts the stall will occur more rapidly than seen in the data. At the two higher reduced frequencies the hysteresis in C_L is very accurate. The C_D comparisons are very good other than the maximum values being slightly underpredicted for the two higher reduced frequencies.

At 8° mean angle of attack, Figures 75 through 80, the results are similar to the S809. The predictions are quite accurate for the lowest reduced frequency, Figures 75 and 76, but become worse as the reduced frequency increases. The open nature of the attached flow hysteresis loops and the premature reattachment result in the prediction error. The attached flow hysteresis being open causes the predicted C_L values to fall below the data for increasing angle of attack, and to be above the data for decreasing angle of attack. Also the C_C attached flow hysteresis are more open, and reattach prematurely, resulting in an underprediction of C_D upon reattachment. Figure 81 illustrates the width of the hysteresis for the lower region and the premature attachment of C_C . Upon reat-

tachment the measured C_C does not lag behind the static data as the model predicts, but instead nearly follows the static data.

Comparisons to CER Data

Figure 82 is a plot of yaw angle versus time as predicted by YawDyn compared to measured data. Time series of wind speed, direction, vertical wind, and vertical and horizontal shears, calculated from the Combined Experiment vertical plane array of anemometers, were used as inputs to YawDyn. As can be seen in the figure the YawDyn comparison with the data is very good and captures all of the features seen in the data.

The yaw angle is well represented by YawDyn, and the normal force coefficient predicted by YawDyn captures the mean quite accurately, but the predicted normal force coefficient lacks the higher frequency components observed in the data, as shown in Figure 83. This is possibly due to the way in which the measured wind is processed for in-

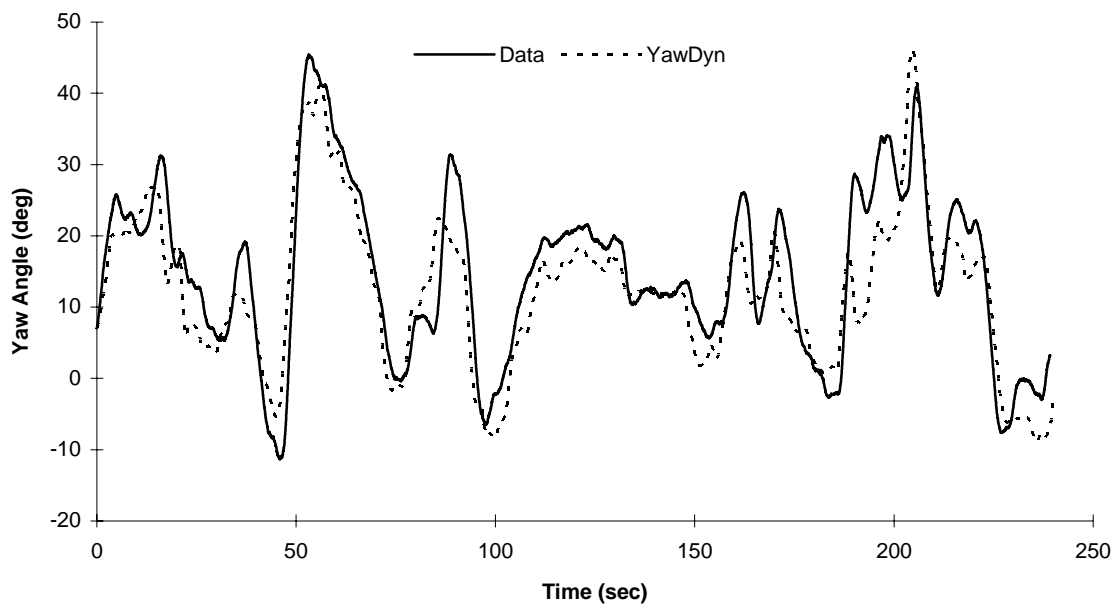


Figure 82: Four minute YawDyn prediction of yaw angle for the CER with a mean wind velocity of 12 m/s, 72 rpm.

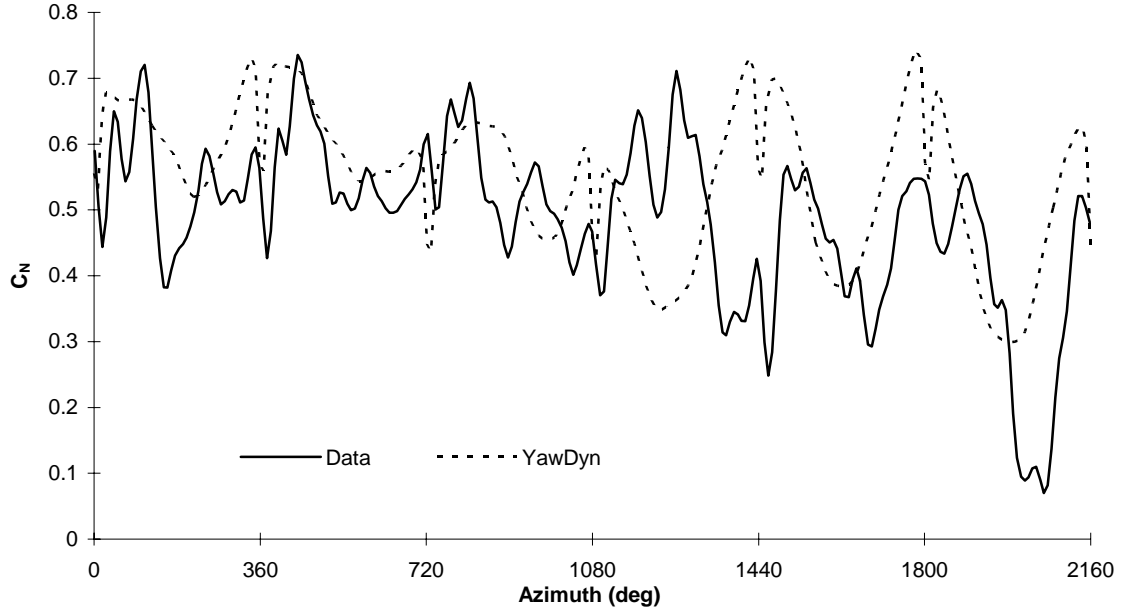


Figure 83: 80% radius normal force coefficient comparison. Conditions as given in Figure 82.

put to AeroDyn. However, for other design codes, or if higher frequency wind data are used in AeroDyn, these higher frequency components may be present, and the aerodynamic model used in these codes should be capable of representing the aerodynamic force coefficients for these higher frequencies. To give an indication of the reduced frequencies seen in the data of Figure 83, the RMS angle of attack versus reduced frequency at the 80% span station is shown in Figure 84. This figure was generated using the entire 4 minutes of data. The once per revolution reduced frequency is $k \approx 0.05$, which corresponds to the largest peak in the figure.

To determine if the Beddoes model was applicable to these higher frequencies, the angle of attack measured from the CER was used as input to the Beddoes subroutines. This permitted examination of only the angle of attack-normal force coefficient relationship, eliminating all rotor dynamics and wind input. Figure 85 is a plot of normal force

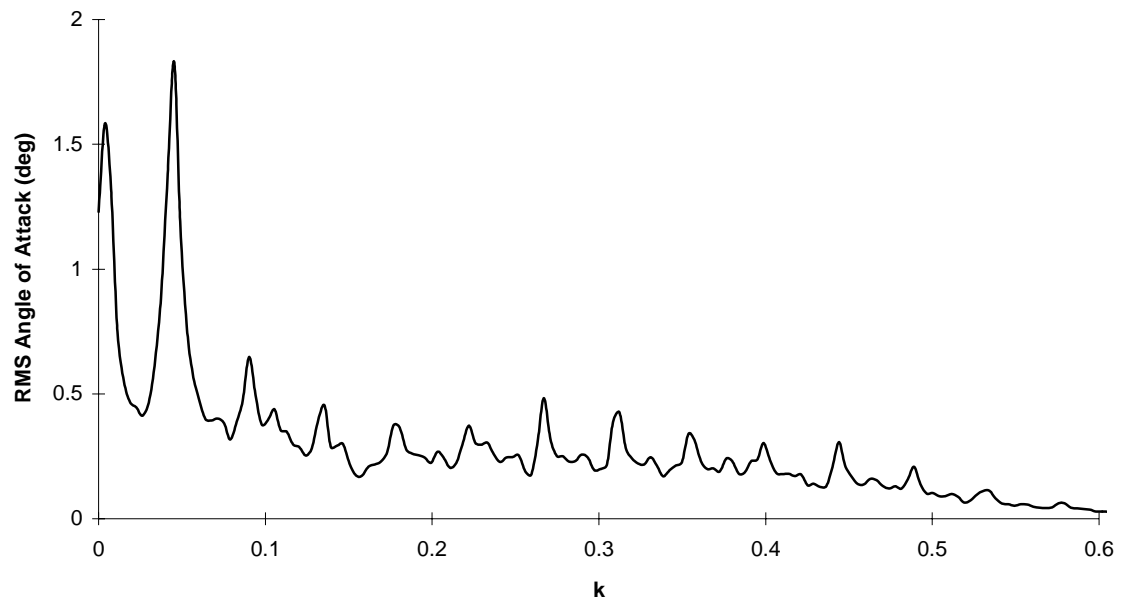


Figure 84: 80% radius root mean square (RMS) angle of attack versus reduced frequency for the four minutes of data used in Figure 82.

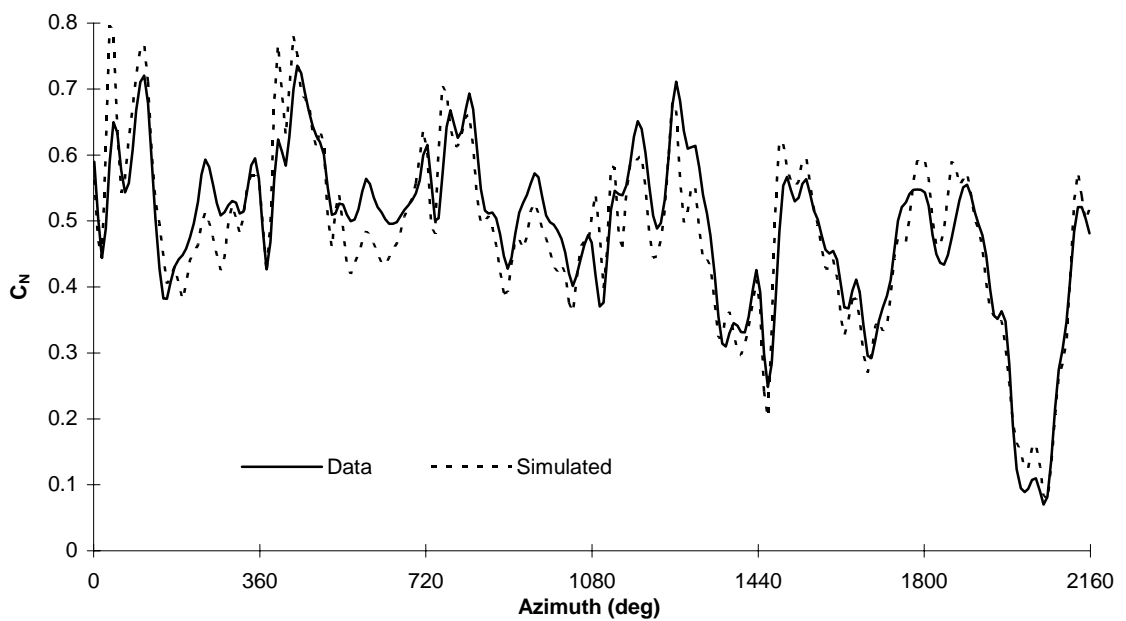


Figure 85: 80% radius normal force coefficient comparison. Conditions as given in Figure 82.

coefficient versus time. Shown in this figure are the normal force coefficient values measured from the CER, and the values predicted using the measured angle of attack from the CER as input to the Beddoes subroutines, labeled in the figure as “simulated.” The simulated curve follows the measured data quite accurately, indicating that the method is capable of accurate normal force predictions for these higher frequencies. It also indirectly indicates that the angle of attack measurement at the outboard stations is quite accurate.

After obtaining good predictions at the outboard blade station, comparisons were then made for the inboard (30%) station. The blades of the CER are untwisted, produc-

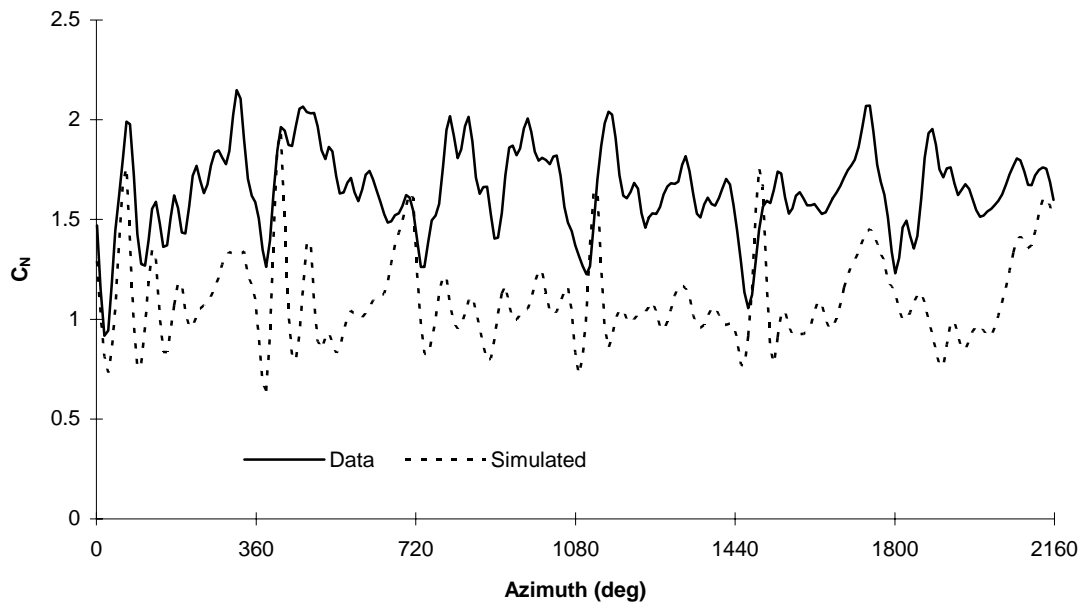


Figure 86: Initial prediction of normal force coefficient at the 30% station. Conditions as given in Figure 82.

ing much higher angles of attack at the inboard station. The initial comparisons are shown in Figure 86. The predicted mean values are much lower than those observed in the data, and in general the comparisons are not very good. To determine why the model

predictions were inaccurate at the inboard station the measured data were studied more closely.

One cause of discrepancy is that at the inboard station the airfoil did not stall as predicted by the static two-dimensional data. This is shown in Figure 87. Notice the measured C_N values stay well above the static line. This is due to the delayed static stall which has been observed by others (Butterfield et al., 1991, Hansen and Butterfield, 1993), and mentioned previously. In an attempt to model this delayed static stall the static curve was modified to pass through the data, as thought to be appropriate. This produced the curve labeled as “modified” in Figure 87.

Also, upon examination of the measured angle of attack at this inboard station, the angle of attack indicator, which is of the vane type, was seen to “ring” (Butterfield, 1989) after the blade passed through the tower shadow. This is shown in Figure 88, where the

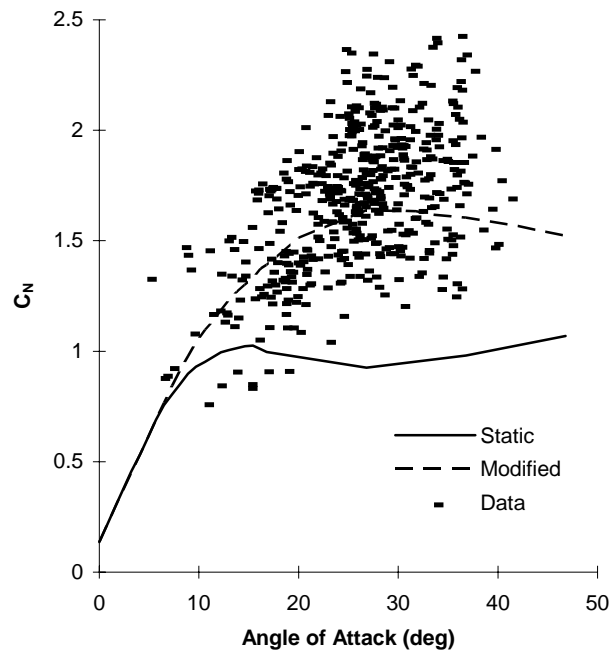


Figure 87: Due to delayed static stall measured operating data remain well above static data.

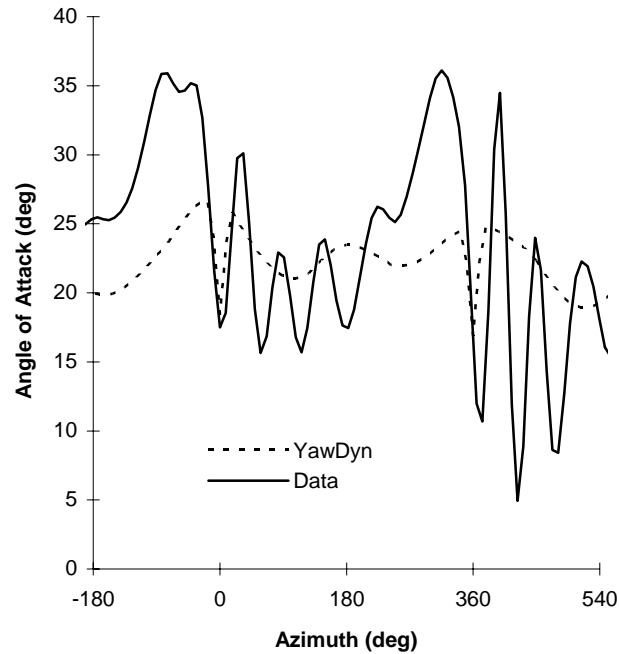


Figure 88: Angle of attack indicator is seen to “ring” after passing through tower shadow.

YawDyn angle of attack prediction is included only to show that the “ringing” does occur after passing through the tower shadow (0 azimuth). Although this ringing was less pronounced at other times in the data, the accuracy of the angle of attack indicator is questionable at this inner station.

However, there was no obvious way of eliminating this ringing from the data. Therefore, the inboard simulation was performed again using the modified static curve, and the measured angle of attack. The results of this simulation are shown in Figure 89. The mean now matches the data quite closely, and many of the features of the data are now represented. Thus it appears that the inboard normal force coefficient can be predicted quite accurately if the static lift curve is modified to account for the delay in stall. Methods for estimating the static lift curve of a rotating blade are the subject of current

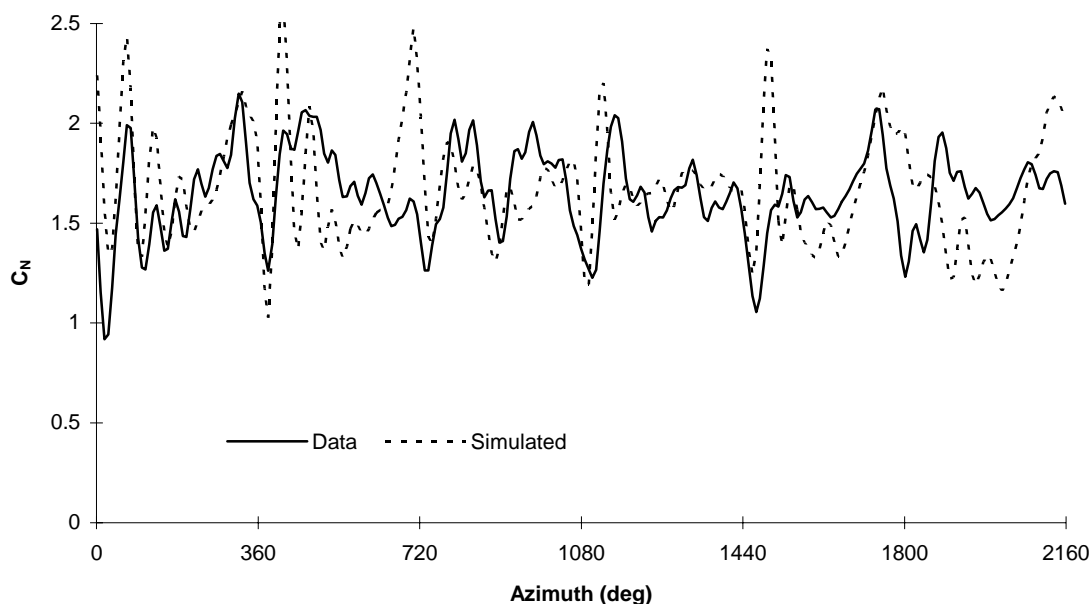


Figure 89: Comparison between predicted and measured normal force coefficients using the modified static curve. Conditions as given in Figure 82.

research (Eggers and Digumarthi, 1992). However, it is encouraging that the dynamic behavior is well represented when the static lift curve is known.

It is of interest to note in Figure 89 that the measured normal force coefficient oscillates at the same frequency seen in the measured angle of attack. This indicates that the angle of attack sensor may be responding to actual fluctuations in angle of attack rather than simply “ringing” after the tower shadow impulse as previously suspected. It does appear that the sensor’s dynamic response exaggerates the angle of attack response, as the oscillations in normal coefficient are smaller than those in angle of attack. No explanation for this observation can be given at this time, and is mentioned as only a point of interest for future investigation.

Sensitivity Studies

Several empirically derived constants are used in the Beddoes model. In general

these constants may be functions of airfoil geometry, Mach number, Reynolds number, or a number of other parameters which may change with varying operating conditions or

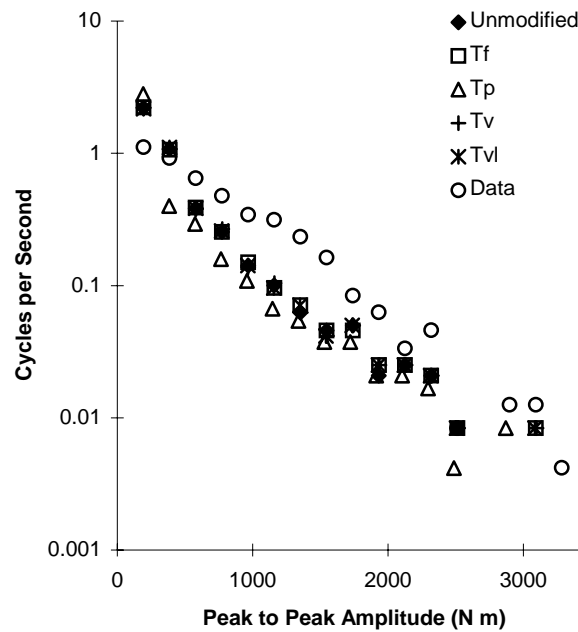


Figure 90: Root flap bending moment rainflow counts for 30% increase in time constants.

The rainflow counts for a 30% decrease in each parameter is shown in Figure 91. For the 30% decrease in each parameter there is no obvious deviation in loading from the unmodified condition.

Thus, it appears that the root flap bending moment predictions are relatively insensitive to changes in the parameters used for the model. Therefore, the constants currently used in the model should not require modification.

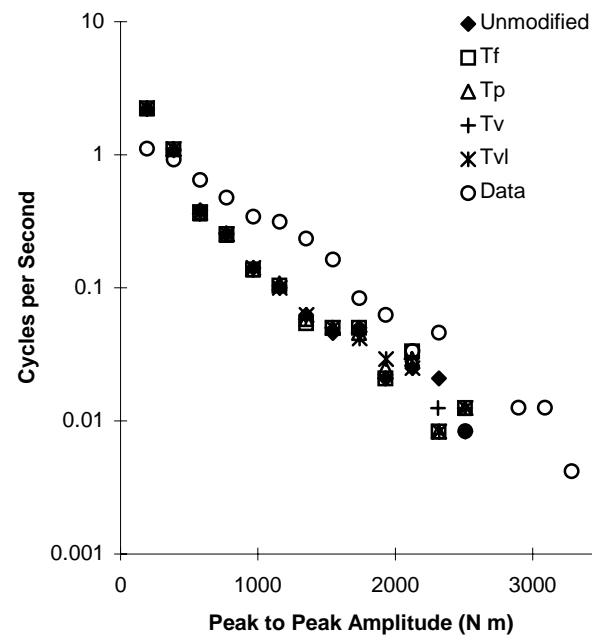


Figure 91: Root flap bending moment rainflow counts for 30% decrease in time constants.

CONCLUSIONS

The Beddoes-Leishman model for unsteady aerodynamics and dynamic stall has been implemented in the University of Utah's AeroDyn subroutines. These subroutines, written in FORTRAN, are used to calculate aerodynamic loading of wind turbines. The storage of calculated effective separation point values in a lookup table, with interpolation between points, together with the use of two effective separation point tables, one for C_N and one for C_C , allow accurate reproduction of static aerodynamic force coefficient values for general inputs of C_L and C_D tables. The above modifications along with angle of attack mirroring about $+90^\circ$ and -90° allow the model to produce dynamic aerodynamic force coefficients over the entire range of angle of attack. Although the accuracy of the model is not known for high or unusual angles of attack, the results obtained seem reasonable.

The model quite accurately reproduces measured two-dimensional unsteady wind tunnel data, given static lift and drag data. The model has been shown to reproduce lift and drag coefficients over a range of reduced frequencies typical of wind turbines, and over a moderate range of angle of attack.

Improvements in the prediction of C_L could be made in the separated region of the hysteresis, where the sharp corners and minimum value are generally missed for the higher reduced frequency, high mean angle of attack cases studied. Also, at times the vortex lift contribution is overestimated, or seems governed by somewhat different dy-

namics. At low mean angles of attack, where the attached flow response is dominant, the attached flow hysteresis loops seem too open for the higher reduced frequency cases used in this study.

Improvements in the C_D predictions could be made for the higher reduced frequency, high mean angle of attack cases studied, where the maximum value and the open nature of the hysteresis for the upper region are at times lacking in the prediction. This is due to the predicted C_C not stalling as rapidly as observed in the data. For the low mean angle of attack, high reduced frequency cases overprediction of C_C results in the C_D prediction falling below the data, at times even becoming negative.

YawDyn prediction of yaw angle using measured wind as input to the CER model is very accurate and possesses all of the features seen in the test data.

The model has been shown to be capable of reproducing the high frequency components of C_N seen in the data measured on the CER at the 80% span when measured angle of attack data are used as input to the dynamic stall routines. Thus the dynamic stall model is appropriate for other wind inputs which may result in higher frequency components of angle of attack, or input of measured angle of attack histories which contain high frequency components.

If the “static lift curve” for a rotating blade may somehow be determined, the model seems capable of quite accurate representation of dynamic delayed stall events.

APPENDIX A

DETERMINATION OF CONSTANTS NEEDED FOR THE MODEL

In addition to the time constants mentioned previously there are several constants associated with the Beddoes-Leishman model which need to be determined from static C_L and C_D data for each airfoil used with the model. The C_N slope near 0° angle of attack ($C_{N\alpha}$), the zero lift angle of attack (α_0), the stall value for positive C_N (C_{N1}), the stall value for negative C_N (C_{N1L}), and the minimum drag C_{D0} , need to be determined.

$C_{N\alpha}$ is best obtained by use of a least squares fit on the linear region of the curve. The least squares fit produces the slope of the curve, $C_{N\alpha}$, and usually the intercept of the curve with the C_N axis ($C_N(\alpha = 0)$). α_0 can then be determined from linear interpolation as:

$$\alpha_0 = \frac{-C_N(\alpha = 0)}{C_{N\alpha}}$$

As the airfoil pitches toward stall the vortex lift is allowed to build. When the current value of the attached flow C_N exceeds C_{N1} the vortex is assumed to convect across the airfoil. For airfoils that have a separation bubble that reattaches, or for airfoils that stall slowly from the trailing edge, it appears that little motion of the airfoil is required to keep the flow attached to the airfoil. Therefore rather than choosing the maximum value of C_N for C_{N1} , the attached flow value of C_N which corresponds to the angle of attack at maximum C_N should be used. This is illustrated in Figures 92 through 94, where the C_{N1} values which resulted in the best unsteady predictions are shown with the data for the three airfoils tested. C_{N1L} is determined in the same way as C_{N1} using the maximum negative value of C_N .

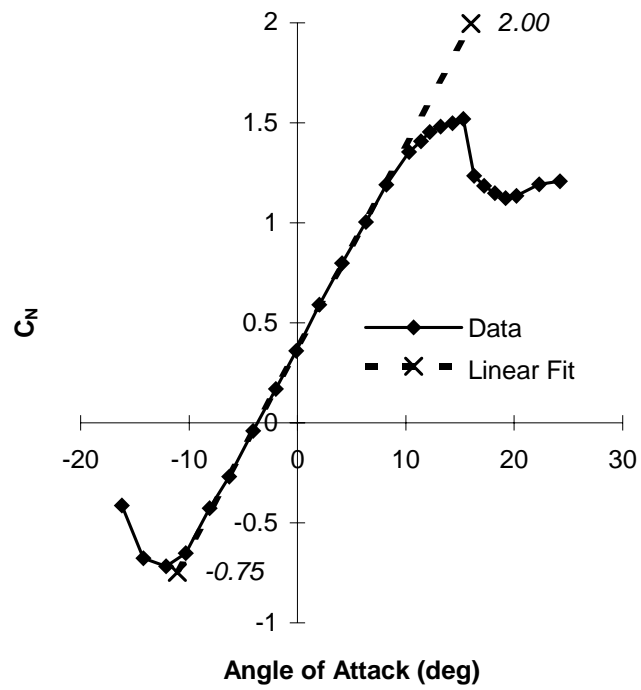


Figure 92: Determination of parameters for the NASA LS(1)-0417 airfoil.

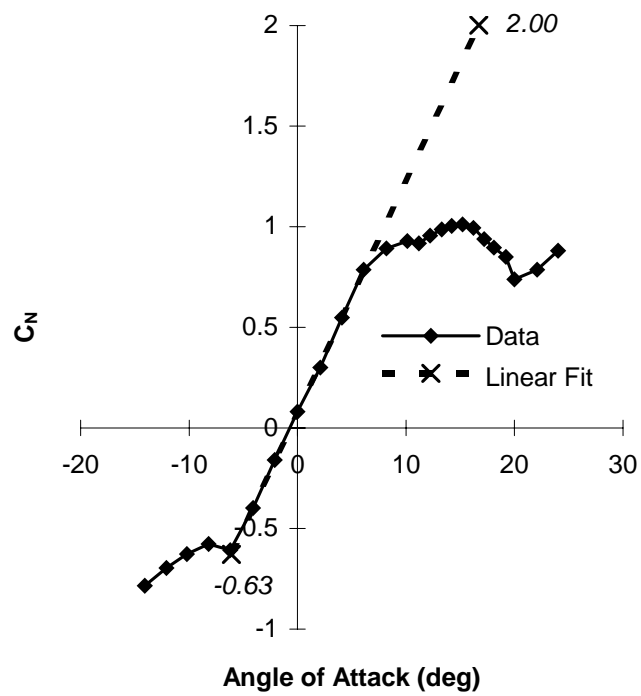


Figure 93: Determination of parameters for the NREL S809 airfoil.

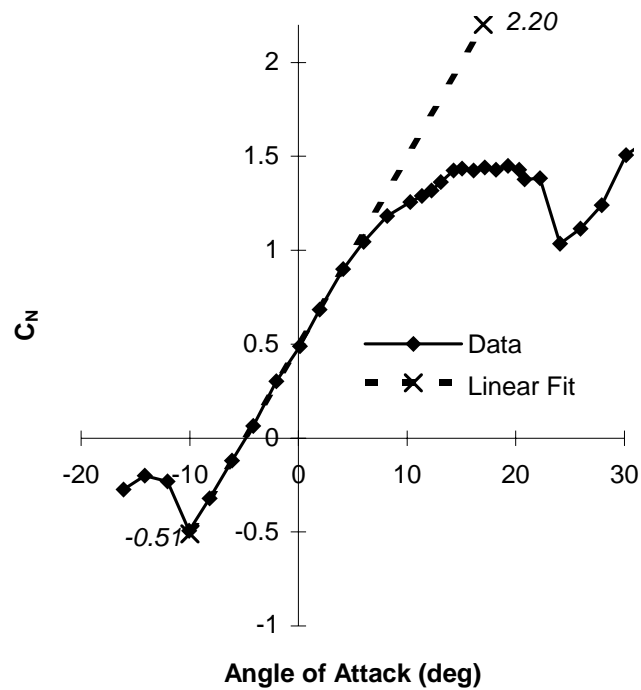


Figure 94: Determination of parameters for the NACA 4415 airfoil.

C_{D0} is the minimum value of drag that occurs near 0° angle of attack.

In addition to determination of the constants above, the separation point curve should be looked at to ensure that it is a somewhat smooth curve. At angles of attack near 0° and α_0 the denominator for determination of the separation point becomes very small. With the denominator approaching zero a small deviation of the aerodynamic coefficients from linear values can result in a large error in the calculation of the separation point. At these times C_L and C_D data may need to be slightly adjusted to produce a relatively smooth curve.

APPENDIX B

FORTRAN PROGRAM DYNSTL

Conversion note: Program listings are not included in this pdf file of Pierce's thesis. See the NREL codes download website for the latest versions of all software.

REFERENCES

- Beddoes, T. S., 1983, "Representation of Airfoil Behavior," *Vertica*, Vol. 7, No. 2, pp. 183-197.
- Beddoes, T. S., 1984, "Practical Computation of Unsteady Lift," *Vertica*, Vol. 8, No. 1, pp. 55-71.
- Bisplinghoff, T. S., Ashley, H., and Halfman, R. L., 1955, *Aeroelasticity*, Addison-Wesley Publishers, Cambridge, MA, pp. 332-353.
- Butterfield, C. P., 1989, "Three Dimensional Airfoil Performance Measurements on a Rotating Wing," Solar Energy Research Institute, SERI Tech. Rep. 217-3505.
- Butterfield, C. P., Huyer, S., and Simms, D., 1991, "Recent Results from Data Analysis of Dynamic Stall on Wind Turbine Blades," Natl. Renewable Energy Lab., NREL Tech. Rep. 257-4654.
- Carr, L. W., 1988, "Progress in the Analysis and Prediction of Dynamic Stall," *Journal of Aircraft*, Vol. 25, No. 1, pp. 6-17.
- Chandrasekhara, M. S., and Carr, L. W., 1990, "Flow Visualization Studies of the Mach Number Effects on Dynamic Stall of an Oscillating Airfoil," *Journal of Aircraft*, Vol. 27, No. 6, pp. 516-522.
- Eggers, A. J., and R. V. Digumarthi, 1992, "Approximate Scaling of Rotational Effects of Mean Aerodynamic Moments and Power Generated By the Combined Experiment Rotor Blades Operating in Deep-Stalled Flow," 11th ASME Wind Energy Symposium, pp. 33-43.
- Gormont, R. E., 1973, "A Mathematical model of Unsteady Aerodynamics and Radial Flow for Application to Helicopter Rotors," U. S. Army Air Mobility Research and Development Laboratory, USAAMRDL Technical Report, 76-67.
- Gregorek, G. M. and Reuss, R. L. 1992, Personal Communication.
- Gregorek, G. M. and Reuss, R. L. 1994, Personal Communication.
- Hansen, A. C., Butterfield, C. P., and Cui, X., 1990, "Yaw Loads and Motions of a Horizontal Axis Wind Turbine," *Journal of Solar Energy Engineering*, Vol. 112, No. 4, pp. 310-314.

Hansen, A. C., 1992, "Yaw Dynamics of Horizontal Axis Wind Turbines: Final Report," Natl. Renewable Energy Lab., NREL Tech. Rep. 442-4822.

Hansen, A. C., and Butterfield, C. P., 1993, "Aerodynamics of Horizontal-Axis Wind Turbines," *Annual Rev. Fluid Mech.*, Vol. 25, pp. 115-149.

Huyer, H., 1993, "Effects of Forced Unsteady Separated Flow Fields on a Rotating Wind Turbine Blade," Natl. Renewable Energy Lab., NREL Tech. Rep. 442-4864.

Leishman, J. G., 1988, "Validation of Approximate Indicial Aerodynamic Functions for Two-Dimensional Subsonic Flow," *Journal of Aircraft*, Vol. 25, No. 10, pp. 914-922.

Leishman, J. G., 1988, "Two Dimensional Model for Airfoil Unsteady Drag Below Stall," *Journal of Aircraft*, Vol. 25, No. 7, pp. 665-666.

Leishman, J. G., 1989, "Modeling Sweep Effects on Dynamic Stall," *Journal of the American Helicopter Society*, Vol. 34, No. 3, pp. 18-29.

Leishman, J. G., 1990, "Modeling of Subsonic Unsteady Aerodynamics for Rotary Wing Applications," *Journal of the American Helicopter Society*, Vol. 35, No. 1, pp. 29-38.

Leishman, J. G. and Beddoes, T. S., 1986, "A Generalized Model For Airfoil Unsteady Behavior and Dynamic Stall Using the Indicial Method," *Proceedings of the 42nd Annual forum of the American Helicopter Society*, Washington D. C., pp. 243-266.

Leishman, J. G. and Beddoes, T. S., 1989, "A Semi-Empirical Model for Dynamic Stall," *Journal of the American Helicopter Society*, Vol. 34, No. 3, pp. 3-17.

Lomax, H. 1960, *AGARD Manual on Aeroelasticity*, Vol. 2, Chapter 6.

McCroskey, W. J., 1981, "The Phenomenon of Dynamic Stall," NASA Technical Memorandum, TM81264.

McCroskey, W. J., 1982, "Unsteady Airfoils," *Annual Rev. Fluid Mech.*, Vol. 14, pp. 285-311.

Osswald, G. A., Ghia, K. N., and Ghia, U. 1991, "Simulations of Dynamic Stall Phenomenon Using Unsteady Navier-Stokes Equations," *Computer Physics Communications*, Vol. 65, pp. 209-218.

Thwaites, B. (ed.), 1960, *Incompressible Aerodynamics*, Oxford University Press, New York, NY, pp. 168-170

Tuncer, I. H., Wu, J. C., and Wang, C. M., 1990, "Theoretical and Numerical Studies of Oscillating Airfoils," *AIAA Journal*, Vol. 28, No. 9, pp. 1615-1624

Tyler, J. C., and Leishman, J. G., 1991, "An Analysis of Pitch and Plunge Effects on Unsteady Airfoil Behavior," *Proceedings of the 47th Annual forum of the American Helicopter Society*, Phoenix AZ.

Wind Energy Program, 1992, "NREL/DOE Combined Experiment Topic Reports from Phase I and Phase II Testing," Natl. Renewable Energy Lab., Compiled January 1992.

Wu, J. C., 1981, "Theory for Aerodynamic Force and Moment in Viscous Flows," *AIAA Journal*, Vol. 19, No 4, pp. 432-441.